

# Vector Similarity Search-Based MCS Selection in Massive Multi-User MIMO-OFDM

Fuga Kobayashi, *Graduate Student Member, IEEE*, Takumi Takahashi, *Member, IEEE*, Shinsuke Ibi, *Senior Member, IEEE*, Takanobu Doi, *Member, IEEE*, Kazushi Muraoka, *Member, IEEE*, and Hideki Ochiai, *Fellow, IEEE*

**Abstract**—This paper proposes a novel modulation and coding scheme (MCS) selection framework that integrates mutual information (MI) prediction based on vector similarity search (VSS) for massive multi-user multiple-input multiple-output orthogonal frequency-division multiplexing (MU-MIMO-OFDM) systems with advanced uplink multi-user detection (MUD). The framework performs MCS selection at the transport block (TB)-level MI and establishes the mapping from post-MUD MI to post-decoding block error rate (BLER) using a prediction function generated from extrinsic information transfer (EXIT) curves. A key innovation is the VSS-based MI prediction scheme, which addresses the challenge of analytically predicting MI in iterative detectors such as expectation propagation (EP). In this scheme, an offline vector database (VDB) stores feature vectors derived from channel state information (CSI) and average received signal-to-noise ratio (SNR), together with corresponding MI values achieved with advanced MUD. During online operation, an approximate nearest neighbor (ANN) search on graphics processing units (GPUs) enables ultra-fast and accurate MI prediction, effectively capturing iterative detection gains. Simulation results under fifth-generation new radio (5G NR)-compliant settings demonstrate that the proposed framework significantly improves both system and user throughput, ensuring that the detection gains of advanced MUD are faithfully translated into tangible system-level performance improvements.

**Index Terms**—MU-MIMO-OFDM systems, iterative detection, expectation propagation, MCS selection, mutual information, vector database, vector similarity search.

## I. INTRODUCTION

Massive multi-user multiple-input multiple-output orthogonal frequency-division multiplexing (MU-MIMO-OFDM) is a key technology to cope with the explosive growth in the number of uplink user equipment (UE) devices in future wireless networks [1]–[3]. Leveraging the large antenna array at the base station (BS) enables multiplexing of uplink traffic from multiple UEs in both spatial and frequency domains, significantly improving spectral efficiency and increasing the number of supported UEs [4]–[6]. To separate these spatially multiplexed signals, the BS requires multi-user detection (MUD) with low complexity and high accuracy [7], [8]. Spatial filtering methods such as zero-forcing (ZF) and linear minimum mean-square error (LMMSE) detection are widely used

for this purpose in MUDs, but their performance degrades as the ratio of transmit streams to the receive antennas increases. Advanced MUD algorithms, offering a better compromise between complexity and performance, have therefore attracted increasing attention [9]–[11].

Maximizing the uplink throughput of MU-MIMO-OFDM systems requires adaptive assignment of the modulation and coding scheme (MCS) index to each UE based on wireless channel quality [12], [13]. A common channel quality metric is the predicted subcarrier-wise signal-to-interference-plus-noise ratio (SINR) achievable with MUD [14]–[16]. The *effective* signal-to-noise ratio (SNR) has also been widely adopted for MCS selection [17], [18]. However, in many standardization specifications [19]–[21], channel coding is applied per transport block (TB), which spans multiple time slots and subcarriers, resulting in a single codeword distributed over time-frequency resources with varying quality. Therefore, it is essential to evaluate TB-level channel quality while accounting for frequency-selective variations. Mutual information (MI), which can be computed per TB, has been recognized as a more suitable metric for this purpose [22]–[24].

With spatial filtering methods such as LMMSE detection, the post-MUD SINR can be analytically estimated from the channel state information (CSI). The estimated subcarrier-wise SINR is then converted to MI, and the predicted MI of the demodulator output is obtained by averaging over all subcarriers within the allocated resource (*i.e.*, one TB). In contrast, with nonlinear iterative detection such as expectation propagation (EP) [25]–[27], analytical estimation of the post-MUD SINR is challenging, since the detection accuracy depends on the convergence behavior of the iterative process [15], [28]. If the MI of the demodulator output cannot be predicted accurately, the gains in MUD performance from iterative detection cannot be fully utilized in MCS selection. Consequently, even if advanced iterative MUD improves link-level detection accuracy, as reported in the literature [29]–[31], it may not translate into higher overall system throughput.

Based on these observations, this paper proposes a novel vector similarity search (VSS)-based offline learning approach for predicting the achievable MI of the demodulator output when using advanced MUD, employing a vector database (VDB) and approximate nearest neighbor (ANN) search [32], [33]. The method consists of two phases: VDB construction via offline learning and online MI prediction using the constructed VDB. In the offline phase, feature vectors (*keys*)—computed from the CSI and average received SNR—are generated and stored in the VDB together with the corresponding MIs (*values*) obtained from actual transmissions over those channels. Repeating this process for numerous channel realizations yields a large-scale key-value stored database. In the online phase, a feature vector is generated

This work was supported in part by JSPS KAKENHI under Grant JP23K13335, JP23K22754, and JP25H01111; in part by JST, CRONOS, Japan under Grant JPMJCS24N1; and in part by MIC/FORWARD under Grant JPMI240710001. (*Corresponding author: Takumi Takahashi.*)

F. Kobayashi, T. Takahashi, and H. Ochiai are with Graduate School of Engineering, The University of Osaka 2-1 Yamada-oka, Suita, 565-0871, Japan (e-mail: kobayashi-f@wcs.comm.eng.osaka-u.ac.jp, {takahashi, ochiai}@comm.eng.osaka-u.ac.jp).

S. Ibi is with Faculty of Science and Engineering, Doshisha University 1-3 Tataramiyakodani, Kyotanabe, 610-0394, Japan (e-mail: sibi@mail.doshisha.ac.jp).

T. Doi and K. Muraoka are with NEC Corporation, 1753 Shimonumabe, Nakahara-ku, Kawasaki, Kanagawa 211-8666, Japan (e-mail: {doi-takanobu, k-muraoka}@nec.com).

from the estimated CSI and average received SNR, and VSS is performed via ANN search on the VDB to retrieve the MI value associated with the most similar key. As this value corresponds to the demodulator output MI achieved for a similar channel, the prediction inherently reflects the convergence characteristics of iterative MUD, enabling high prediction accuracy. ANN search has been employed to perform accurate VSS by exploiting similarities or correlations in the data [34] and has been developed in fields such as cross-language translation and high-dimensional image classification [32], [33]. Recently, high-speed ANN libraries capable of executing search algorithms on graphics processing units (GPUs), such as Faiss [35], Milvus [36], and SONG [37], have emerged. Leveraging these advances, ANN search has been applied to wireless communication problems, including transmission power allocation [38] and meta-learning for deep unfolding (DU)-aided signal detection [39]. This study can be considered an extension of such applications, targeting MI prediction for advanced iterative MUD.

The main contributions of this work are as follows:

- A novel VSS-based MI prediction method is developed for EP-based iterative detection<sup>1</sup>. The VDB stores feature vectors computed from the CSI and average received SNR, paired with the measured MI obtained via EP detection. During prediction, VSS retrieves the MI that corresponds to the most similar feature vector using ANN search. To further enhance prediction accuracy, the MI values corresponding to multiple high-similarity vectors can be averaged—referred to as the top- $K$  method. Simulation results demonstrate that the proposed approach achieves high prediction accuracy even with iterative MUD, addressing the limitations of conventional SINR-based prediction methods.
- The decoding characteristics of the channel decoder for each MCS index described in the fifth-generation new radio (5G NR) standard are modeled using extrinsic information transfer (EXIT) functions [40], [41]. The decoding behavior is represented by an EXIT curve, which relates the MI between the decoder input and output. By replacing the decoder output MI with the post-decoding block error rate (BLER) in the EXIT curve, the post-decoding BLER can be predicted from the input MI without performing actual decoding. Simulations demonstrate highly accurate prediction of decoding characteristics.
- An MI-based MCS selection framework is established by integrating the above two methods. For each modulation scheme, MI values are predicted using the VDB and ANN search based on the estimated CSI. The achievable post-decoding BLER is then obtained from the predicted MI via EXIT curves. For each UE, the highest MCS index that satisfies the target (reference) BLER is selected, illustrating the performance gains achieved through EP-based advanced MUD.
- Comprehensive evaluations are conducted, demonstrating significant improvements in both system and user throughput compared with conventional SINR-based schemes. The results highlight the importance of selecting MCS according to the actual detection performance. An

MCS selection strategy that incorporates the improved performance of advanced iterative MUD yields substantial throughput benefits. Analysis of the selected MCS indices under varying channel conditions provides quantitative evidence of the adaptability of the method and its ability to optimize overall system performance.

To our knowledge, no previous work has proposed an MCS selection framework for massive MU-MIMO-OFDM systems that can assess channel quality while accounting for convergence characteristics of advanced iterative MUD. Although numerous studies have improved MUD performance in link-level simulations using iterative detection, many such simulations rely on idealized conditions that differ substantially from practical wireless environments. This work bridges that gap, serving as a crucial first step toward translating theoretical advances in iterative MUD into tangible performance gains in real-world wireless communication systems.

The remainder of this paper is organized as follows. Section II describes the system model. Section III presents the MCS selection framework using LMMSE filtering as MUD, where functionalizing decoder characteristics via EXIT analysis under the 5G NR standard constitutes a novel contribution. It also demonstrates that LMMSE-based MUD enables analytically accurate MI prediction and identifies the challenges posed by EP-based iterative MUD. Section IV addresses these challenges by introducing a VSS-based MI prediction method that accurately estimates post-MUD MI for EP-based MUD. Section V integrates these techniques into the MCS selection framework and demonstrates significant improvements in system and user throughput. Section VI discusses the feasibility and performance implications of the proposed method using dynamic system-level simulations that incorporate long-term variations in channel statistics, integration with outer-loop link adaptation (OLLA), and scheduling mechanisms for resource allocation. Section VII concludes the paper.

*Notation:* Sets of real and complex numbers are denoted by  $\mathbb{R}$  and  $\mathbb{C}$ , respectively. Vectors are represented by lower-case boldface letters, and matrices by upper-case boldface letters. The transpose and conjugate transpose operators are denoted by  $\cdot^T$  and  $\cdot^H$ , respectively. The  $a \times a$  identity matrix is represented by  $I_a$ . A diagonal matrix with elements of the vector  $\mathbf{a}$  on its main diagonal is denoted by  $\text{diag}[\mathbf{a}]$ . The element in the  $i$ -th row and  $j$ -th column of matrix  $\mathbf{A}$  is denoted by  $[\mathbf{A}]_{i,j}$ . A complex Gaussian distribution with mean  $a$  and variance  $b$  is denoted by  $\mathcal{CN}(a, b)$ . Finally, the notation  $\mathcal{O}(\cdot)$  denotes the complexity order unless otherwise specified.

#### A. Related Works

To the best of our knowledge, there is no prior work that explicitly translates the iterative gain achieved by iterative detectors into throughput improvement through advanced MCS selection. Although theoretical studies focusing on the behavior analysis of detectors themselves, as well as practical studies dedicated to link adaptation, have been reported so far, research that integrates these two aspects remains scarce, despite its fundamental importance.

For example, advanced iterative detectors, including EP, have historically evolved alongside asymptotic performance analyzes in the large-system limit, and a vast body of literature exists on their asymptotic optimality [26], [27]. However, such

<sup>1</sup>While the proposed framework can be applied to arbitrary MUD schemes, we adopt EP as an initial study because of its strong theoretical foundation, excellent practical performance, and stable convergence [26], [27].

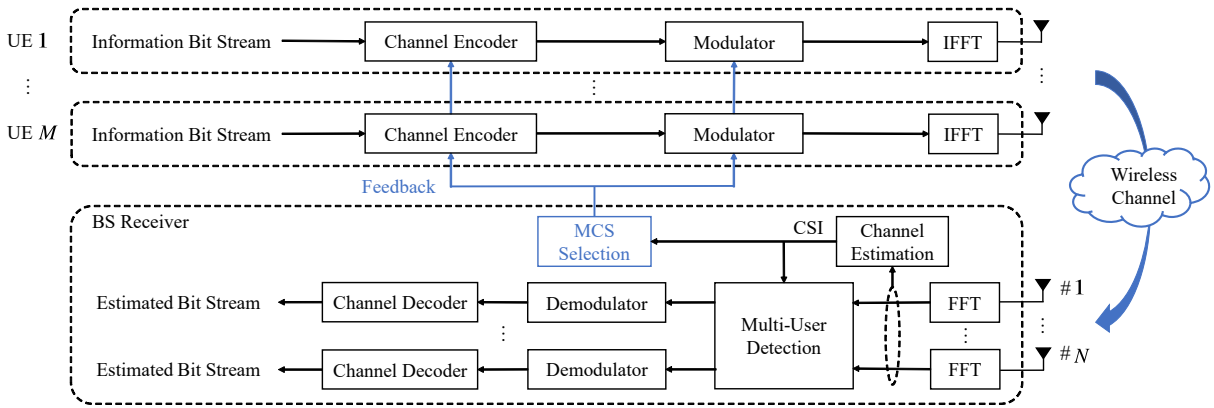


Fig. 1. Block diagram of the MU-MIMO-OFDM system, where the MCS selection stage is highlighted in blue.

asymptotic analyzes cannot be directly applied to the statistically non-uniform and practically important finite-dimensional systems considered in this study. In particular, it is intrinsically difficult to predict the convergence behavior in advance in environments where multiple modulation schemes coexist.

On the other hand, learning-based MCS selection has been extensively studied using Q-learning-based approaches [42], [43], where a Q-table is iteratively updated to maximize the expected long-term reward for each MCS. However, because the Q-table size grows exponentially with the state dimension, such methods become impractical for large-scale or continuous state spaces, restricting their applicability to small state-action spaces. To alleviate this scalability issue, deep Q-network (DQN)-based methods employing deep neural networks (DNNs) to approximate the Q-function have been proposed [44]–[47]. While these methods can handle high-dimensional continuous state spaces without explicitly storing a Q-table, they also introduce inherent drawbacks, including increased learning complexity, sensitivity to channel variations and hyperparameters, and a lack of theoretical guarantees on convergence and stability. Moreover, their focus on single-link adaptation and global optimization under diverse channel conditions limits their applicability to large-scale systems with stringent latency constraints.

In contrast, the approach proposed in this study is fundamentally different. By leveraging instantaneous CSI and average received SNR as key features and significantly reducing the search space through offline learning, the proposed method enables fast and accurate MI prediction and instantaneous channel-aware MCS selection even in massive MU-MIMO-OFDM systems. The approach can be regarded as offloading the complex processing task to the offline domain. Furthermore, the VDB supports efficient updates by adding or removing data entries as long-term channel statistics change, eliminating the need for retraining.

## II. SYSTEM MODEL

### A. Signal Model

Consider an uplink massive MU-MIMO-OFDM system conforming to the 5G NR specification, as illustrated in Fig. 1. Each UE has one transmit (TX) antenna, and  $M$  UEs perform spatial multiplexing to a BS equipped with  $N$  receive (RX) antennas arranged in a uniform rectangular array (URA). Based on the acquired CSI, the BS performs resource allocation and MCS selection for uplink transmission

and feeds back the results to each UE. Each UE encodes and modulates its information bit stream using the selected MCS, then transmits the signal via OFDM over the allocated time–frequency resources. In 5G NR [48], the smallest TB is a resource block (RB) consisting of 14 OFDM symbols (time)  $\times$  12 subcarriers (frequency). In this work,  $M$  UEs are assumed to perform spatial multiplexing transmission over time–frequency resources consisting of  $R$  OFDM symbols and  $L$  subcarriers, as determined by resource allocation; thus, we focus on the transmission of a single TB containing  $R \times L$  symbols. The cyclic prefix is assumed to be ideally inserted and removed. At the receiver, frequency-domain MIMO signal detection is performed via MUD, followed by demodulation and channel decoding.

Let  $x_m[r, \ell]$  denote the frequency-domain symbol transmitted by the  $m$ -th UE at discrete time  $r$  on the subcarrier  $\ell$ . Each symbol is drawn from the quadrature amplitude modulation (QAM) constellation  $\mathcal{X}$  with average energy  $E_s$  and modulation order  $Q \triangleq |\mathcal{X}|$ . Denoting the TX vector spatially multiplexed on the  $[r, \ell]$ -th time-frequency resource by  $\mathbf{x}[r, \ell] \triangleq [x_1[r, \ell], \dots, x_m[r, \ell], \dots, x_M[r, \ell]]^T \in \mathbb{C}^{M \times 1}$ , the corresponding RX vector can be expressed as

$$\begin{aligned} \mathbf{y}[r, \ell] &\triangleq [y_1[r, \ell], \dots, y_n[r, \ell], \dots, y_N[r, \ell]]^T \in \mathbb{C}^{N \times 1} \\ &= \mathbf{H}[\ell] \mathbf{x}[r, \ell] + \mathbf{z}[r, \ell], \end{aligned} \quad (1)$$

where  $\mathbf{H}[\ell] \triangleq [\mathbf{h}_1[\ell], \dots, \mathbf{h}_m[\ell], \dots, \mathbf{h}_M[\ell]] \in \mathbb{C}^{N \times M}$  denotes the frequency-domain MIMO channel matrix of the  $\ell$ -th subcarrier, with  $\mathbf{h}_m[\ell] \in \mathbb{C}^{N \times 1}$  representing its  $m$ -th column. The channel is assumed to be constant over one time slot ( $1 \leq r \leq R$ ), and  $\mathbf{z}[r, \ell] \triangleq [z_1[r, \ell], \dots, z_n[r, \ell], \dots, z_N[r, \ell]]^T \in \mathbb{C}^{N \times 1}$  is the additive white Gaussian noise (AWGN) vector, each entry of which follows  $\mathcal{CN}(0, N_0)$  with  $N_0$  denoting the noise power spectral density.

Since the MCS for each UE must be determined prior to actual transmission, the BS predicts the achievable demodulator output MI under MUD using the estimated CSI  $\mathbf{H}[\ell], \forall \ell$ , and the average received SNR  $\rho \triangleq M E_s / N_0$ , without relying on the RX signal  $\mathbf{y}[r, \ell], \forall r, \forall \ell$ . For simplicity, both the CSI  $\mathbf{H}[\ell], \forall \ell$  and average received SNR  $\rho$  are assumed to be perfectly estimated at the BS, and the assigned MCS index is assumed to be notified to each UE without error.

**Algorithm 1** EP-based MUD algorithm

**Require:**  $\mathbf{y} \in \mathbb{C}^{N \times 1}$ ,  $\mathbf{H} \in \mathbb{C}^{N \times M}$ ,  $T$  (Num. of iterations)

**Ensure:**  $q_{m,A \rightarrow B}^{(T)}(\chi), \forall m, \forall \chi \in \mathcal{X}$ 


---

```

/* ----- Initialization ----- */
1:  $\mathbf{x}_{B \rightarrow A}^{(1)} = \mathbf{0} \in \mathbb{C}^{M \times 1}$ ,  $\mathbf{V}_{B \rightarrow A} = E_s \mathbf{I}_M$ 
/* ----- Iteration ----- */
2: for  $t = 1$  to  $T$  do
    // Module A
3:  $\boldsymbol{\Psi}^{(t)} = (N_0 \mathbf{I}_N + \mathbf{H} \mathbf{V}_{B \rightarrow A}^{(t)} \mathbf{H}^H)^{-1}$ 
4:  $\boldsymbol{\Xi}^{(t)} = (\text{diag} [\mathbf{h}_1^H \boldsymbol{\Psi}^{(t)} \mathbf{h}_1, \dots, \mathbf{h}_M^H \boldsymbol{\Psi}^{(t)} \mathbf{h}_M])^{-1}$ 
5:  $\mathbf{x}_{A \rightarrow B}^{(t)} = \mathbf{x}_{B \rightarrow A}^{(t)} + \boldsymbol{\Xi}^{(t)} \mathbf{H}^H \boldsymbol{\Psi}^{(t)} (\mathbf{y} - \mathbf{H} \mathbf{x}_{B \rightarrow A}^{(t)})$ 
6:  $\mathbf{V}_{A \rightarrow B}^{(t)} = \boldsymbol{\Xi}^{(t)} - \mathbf{V}_{B \rightarrow A}^{(t)}$ 
7:  $\forall m, \forall \chi \in \mathcal{X} : q_{m,A \rightarrow B}^{(t)}(\chi) = \exp \left( -\frac{|\chi - x_{m,A \rightarrow B}^{(t)}|^2}{v_{m,A \rightarrow B}^{(t)}} \right)$ 
    // Module B
8:  $\forall m : x_{m,B}^{(t)} = \frac{\sum_{\chi \in \mathcal{X}} \chi \cdot q_{m,A \rightarrow B}^{(t)}(\chi)}{\sum_{\chi' \in \mathcal{X}} q_{m,A \rightarrow B}^{(t)}(\chi')}$ 
9:  $\forall m : v_{m,B}^{(t)} = \frac{\sum_{\chi \in \mathcal{X}} |\chi|^2 \cdot q_{m,A \rightarrow B}^{(t)}(\chi)}{\sum_{\chi' \in \mathcal{X}} q_{m,A \rightarrow B}^{(t)}(\chi')} - |x_{m,B}^{(t)}|^2$ 
10:  $\forall m : \frac{1}{\bar{v}_{m,B \rightarrow A}^{(t)}} = \frac{1}{v_{m,B}^{(t)}} - \frac{1}{v_{m,A \rightarrow B}^{(t)}}$ 
11:  $\forall m : \bar{x}_{m,B \rightarrow A}^{(t)} = \bar{v}_{m,B \rightarrow A}^{(t)} \cdot \left( \frac{x_{m,B}^{(t)}}{v_{m,B}^{(t)}} - \frac{x_{m,A \rightarrow B}^{(t)}}{v_{m,A \rightarrow B}^{(t)}} \right)$ 
12:  $\bar{\mathbf{x}}_{B \rightarrow A}^{(t)} = [\bar{x}_{1,B \rightarrow A}^{(t)}, \dots, \bar{x}_{m,B \rightarrow A}^{(t)}, \dots, \bar{x}_{M,B \rightarrow A}^{(t)}]^T$ 
13:  $\bar{\mathbf{V}}_{B \rightarrow A}^{(t)} = \text{diag} [\bar{v}_{1,B \rightarrow A}^{(t)}, \dots, \bar{v}_{m,B \rightarrow A}^{(t)}, \dots, \bar{v}_{M,B \rightarrow A}^{(t)}]$ 
14:  $\mathbf{x}_{B \rightarrow A}^{(t+1)} = \alpha \bar{\mathbf{x}}_{B \rightarrow A}^{(t)} + (1 - \alpha) \mathbf{x}_{B \rightarrow A}^{(t)}$ 
15:  $\mathbf{V}_{B \rightarrow A}^{(t+1)} = \alpha \bar{\mathbf{V}}_{B \rightarrow A}^{(t)} + (1 - \alpha) \mathbf{V}_{B \rightarrow A}^{(t)}$ 
16: end for

```

---

**B. EP-based MUD Algorithm**

The pseudocode of the EP-based MUD algorithm, designed following [9], [25]–[27], is given in Algorithm 1. For clarity, the qualifier  $[r, \ell]$  is omitted since MUD is performed independently for each time–frequency index. The following notation is used:  $\mathbf{x}_\zeta \triangleq [x_{1,\zeta}, \dots, x_{m,\zeta}, \dots, x_{M,\zeta}]^T$ ,  $\mathbf{V}_\zeta \triangleq \text{diag} [v_{1,\zeta}, \dots, v_{m,\zeta}, \dots, v_{M,\zeta}]$ , where  $\zeta \in \{A \rightarrow B, B \rightarrow A\}$ . The EP detector comprises module A, which applies soft interference cancellation and signal separation using an LMMSE filter, and module B, which computes the conditional expectation—*i.e.*, the general minimum mean-square error (MMSE) solution—based on the output of module A. Detection accuracy improves progressively through the exchange of extrinsic information between the two modules. Further algorithmic details can be found in [9], [25]–[27]. The number of iterations is denoted by  $T$ , and  $(\cdot)^{(t)}$  indicates the iteration index. The parameter  $\alpha$  in lines 14 and 15 is a damping factor. When  $T = 1$ , Algorithm 1 reduces to the conventional LMMSE detector.

**C. Computation of Bit-Wise LLRs**

Continuing from the previous subsection, the qualifier  $[r, \ell]$  is omitted. Based on the message  $q_{m,A \rightarrow B}^{(T)}(\chi)$  from module A to B in the final iteration of Algorithm 1, the log-likelihood ratios (LLRs) of the coded bits composing the TX symbol  $x_m$

are computed. When  $x_m$  consists of  $S \triangleq \log_2 Q$  coded bits  $c_{m,1}, \dots, c_{m,s}, \dots, c_{m,S}$ , the bit-wise LLR corresponding to  $c_{m,s}$  is given by [49]

$$\lambda(c_{m,s}) \triangleq \ln \left[ \frac{\sum_{\chi \in \mathcal{X} | c_s=1} q_{m,A \rightarrow B}^{(T)}(\chi)}{\sum_{\chi' \in \mathcal{X} | c_s=0} q_{m,A \rightarrow B}^{(T)}(\chi')} \right], \quad (2)$$

where  $\mathcal{X} | c_s = c$  ( $c \in \{0, 1\}$ ) denotes the set of candidate constellation points whose  $s$ -th bit equals  $c$ .

**D. MI Computation per TB**

Let  $\lambda$  denote the bit-wise LLR corresponding to the coded bit  $c$ . The bit-wise MI between  $c$  and  $\lambda$  at the demodulator output LLRs can then be expressed as [40]

$$I(\lambda; c) = \sum_{c \in \{0,1\}} p_c(c) \int_{-\infty}^{\infty} p_{\lambda|c}(\lambda | c) \log_2 \left( \frac{p_{\lambda|c}(\lambda | c)}{\sum_{c' \in \{0,1\}} p_c(c') p_{\lambda|c'}(\lambda | c')} \right) d\lambda. \quad (3)$$

With the qualifier  $[r, \ell]$ , the detector output LLRs for the coded bits composing  $x_m[r, \ell]$  are denoted by  $\lambda(c_{m,s})[r, \ell], \forall s$ , as given in (2). The total number of coded bits in one TB is  $N_{\text{TB}} = R \times L \times S$ . Using all corresponding LLRs, the demodulator output MI in (3) can be approximated as [50]

$$I_{m,\text{TB}} \approx 1 - \frac{1}{N_{\text{TB}}} \sum_{r=1}^R \sum_{\ell=1}^L \sum_{s=1}^S \eta_{m,s}[r, \ell], \quad (4a)$$

$$\eta_{m,s}[r, \ell] \triangleq \log_2 (1 + \exp[-(2c_{m,s}[r, \ell] - 1)\lambda(c_{m,s})[r, \ell]]), \quad (4b)$$

where  $c_{m,s}[r, \ell]$  denotes the coded bit corresponding to  $\lambda(c_{m,s})[r, \ell]$ , which consists of the TX symbol  $x_m[r, \ell]$  in (1).

A key point to note is that MCS selection must be completed prior to transmission; thus, the demodulator output MI  $I_{m,\text{TB}}$  in (4) must be predicted solely based on the estimated CSI and average received SNR. For determining the MCS, the predicted MI is then converted to the decoder output BLER according to the decoding characteristics. It is only through this two-stage process—MI prediction followed by BLER conversion—that the MCS can be appropriately selected.

In the following section, we present the MI-based MCS selection framework, which is one of the main contributions of this work, using LMMSE-based MUD as a representative example.

**III. MI-BASED MCS SELECTION**

Fig. 2 illustrates the block diagram of the MI-based MCS selection procedure using the analytical MI prediction method. In this scheme, the BS determines the appropriate MCS for each UE from the estimated CSI and the averaged received SNR. The process comprises three steps: (i) predicting the demodulator output (*i.e.*, post-MUD) MI for all modulation schemes predefined in the MCS table, (ii) converting each predicted post-MUD MI to the corresponding post-decoding BLER according to the specific decoding characteristics, and (iii) selecting the MCS index that maximizes throughput while satisfying the reference BLER. Note that since MI depends on the modulation scheme, the step (i) must be performed individually for each scheme. The detailed procedure is presented below, where the LMMSE filter is employed as MUD.

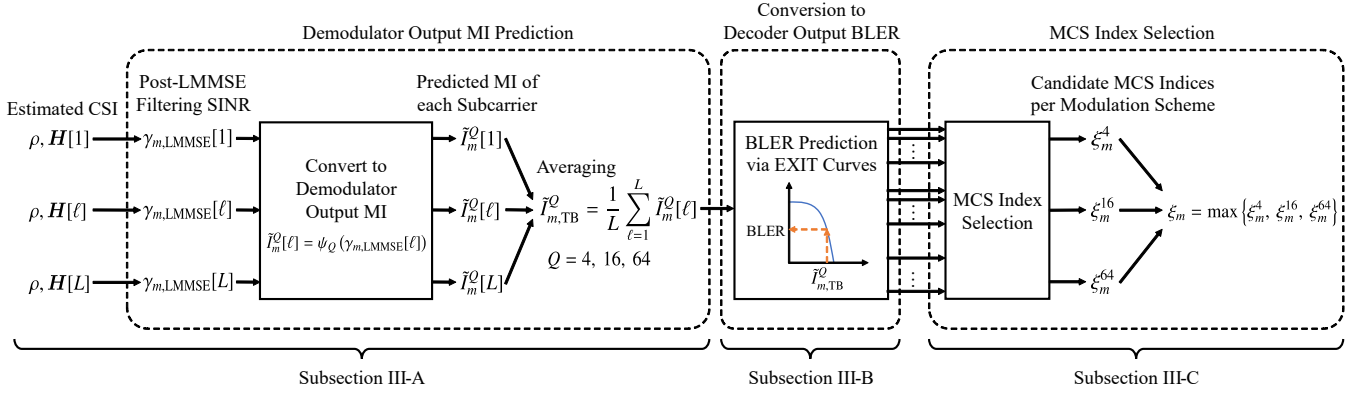


Fig. 2. Block diagram of the proposed MI-based MCS selection process incorporating the analytical MI prediction method.

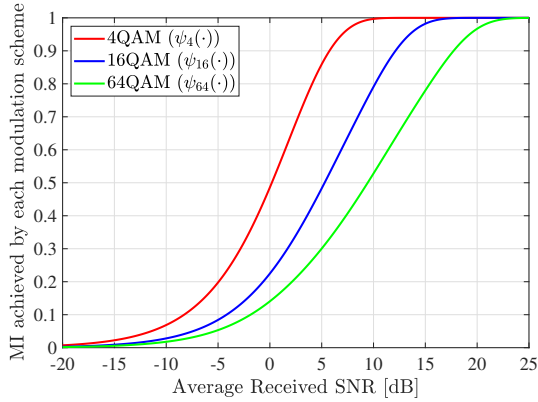


Fig. 3. Average received SNR versus MI in an AWGN channel.

### A. Analytical MI Prediction for LMMSE Filter Output

When employing the LMMSE filter as MUD, the post-MUD SINR can be derived analytically. For detecting  $x_m[r, \ell]$ ,  $\forall r$ , from the RX signal  $\mathbf{y}[r, \ell]$ ,  $\forall r$ , in (1), the SINR at the LMMSE filter output can be expressed in closed-form as [51]

$$\gamma_{m,\text{LMMSE}}[\ell] = \frac{1}{\left[ (\rho \mathbf{H}^H[\ell] \mathbf{H}[\ell] + \mathbf{I}_M)^{-1} \right]_{m,m}} - 1. \quad (5)$$

Next, by modeling the LMMSE filter output as the output of an AWGN channel with the same SNR as in (5), the post-MUD SINR for each subcarrier can be converted to the predicted demodulator output MI as  $\tilde{i}_m^Q[\ell] = \psi_Q(\gamma_{m,\text{LMMSE}}[\ell])$ , where  $\psi_Q(\cdot)$ , with  $Q \in \{4, 16, 64\}$ , is the conversion function shown in Fig. 3. By averaging over all  $L$  subcarriers, the predicted demodulator output MI  $I_{m,\text{TB}}$  in (4) can be expressed as

$$\tilde{i}_{m,\text{TB}}^Q = \frac{1}{L} \sum_{\ell=1}^L \tilde{i}_m^Q[\ell], \quad \forall Q. \quad (6)$$

For MCS selection, the post-MUD MIs are first computed using (6) for all modulation orders. Each predicted MI is then converted to the corresponding decoder output MI according to the decoding characteristics, and the highest MCS index meeting the reference BLER is selected.

### B. Conversion to Decoder Output BLER

The decoding characteristics are modeled using EXIT curves [50], [52], [53]. Traditionally, these curves are obtained

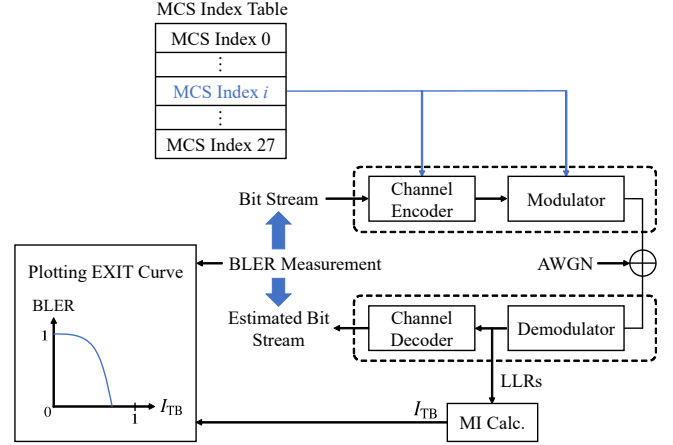


Fig. 4. Block diagram for measuring the relationship between the demodulator output MI and the decoder output BLER in an AWGN channel.

by generating ideal LLR sequences that satisfy the consistency condition<sup>2</sup> [41] and measuring the decoder input–output MI. However, for higher-order modulation schemes (e.g., 16QAM, 64QAM), the decoder input LLRs deviate from the ideal statistics due to the non-orthogonal mapping between bits and constellation points [49]. This mismatch causes the MI observed in practice to differ from that predicted by the ideal EXIT curve. In addition, for MCS selection, the relevant metric is the decoder output BLER, not MI. Consequently, unlike conventional EXIT curves, which focus solely on MI, the derived curves must capture BLER characteristics to enable accurate MCS selection.

To ensure accurate conversion from predicted post-MUD MI to decoder output BLER (post-decoding BLER), we derive EXIT curves using the procedure illustrated in Fig. 4, which reflects the actual LLR statistics for each MCS index:

- 1) Simulation Setup: Generate coded symbols according to the target MCS index.
- 2) Channel Modeling: Pass the symbols through an AWGN channel adjusted to achieve the desired input MI.
- 3) LLR Computation: Obtain demodulator output LLRs directly from the channel output, preserving their actual statistical distribution.
- 4) Decoder Evaluation: Measure the decoder input MI from

<sup>2</sup>The distribution of ideal LLRs satisfying the consistency condition is the Gaussian distribution with the mean  $\mu$  and the variance  $\sigma^2 = 2\mu$ .

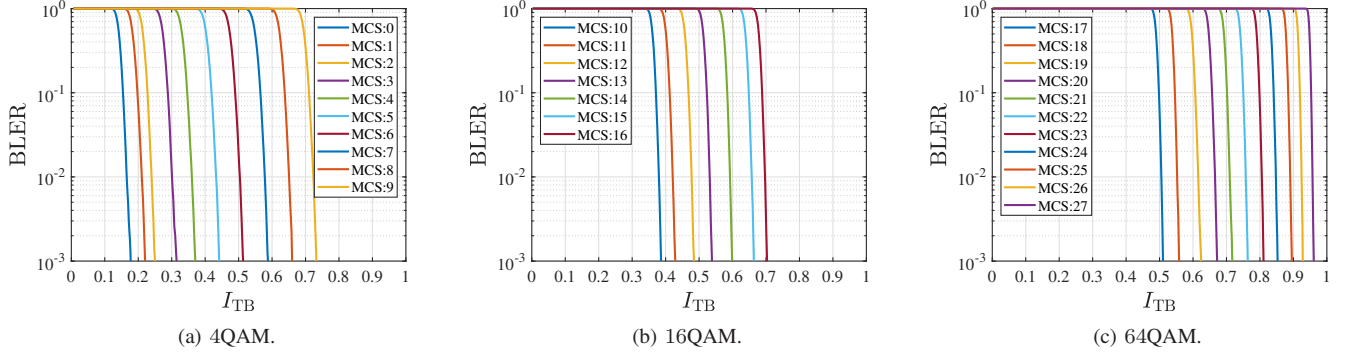
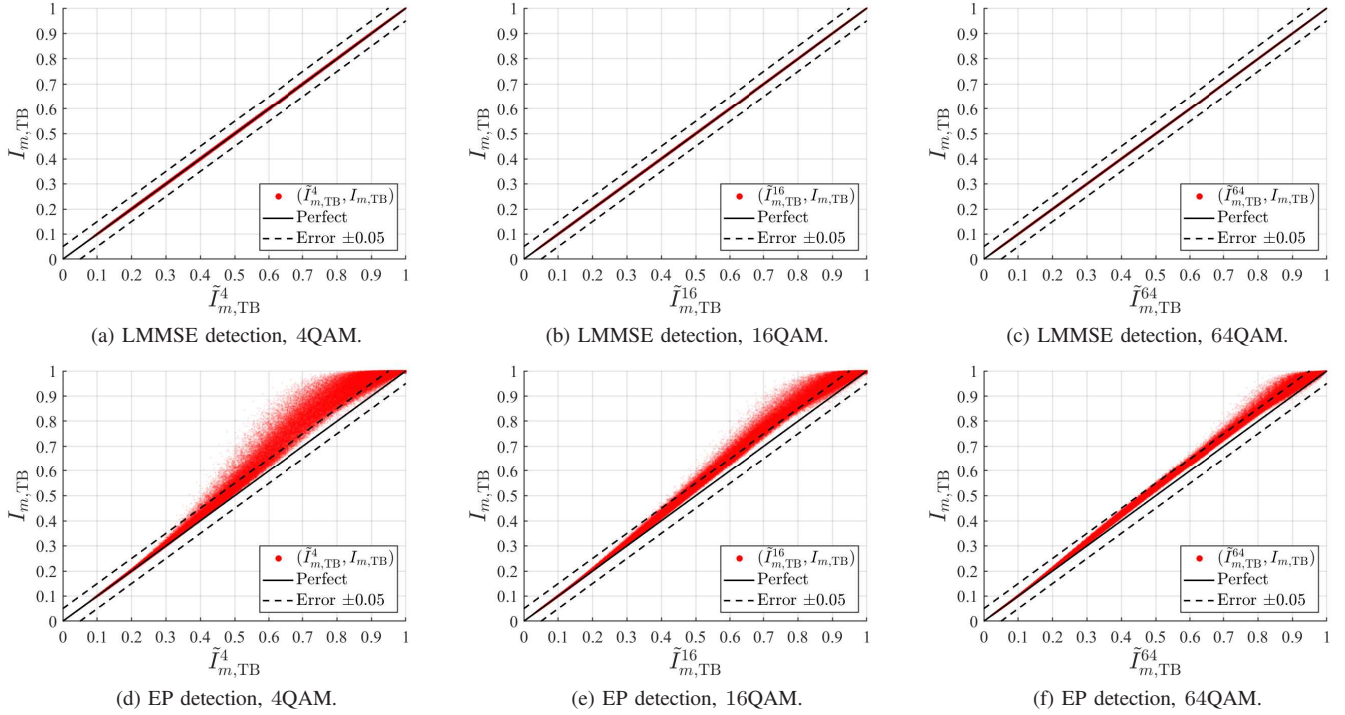

 Fig. 5. EXIT curves showing decoder input MI  $I_{m,TB}$  versus BLER for each MCS.

 Fig. 6. Scatter plots of the measured MI  $I_{m,TB}$  versus the predicted MI  $\tilde{I}_{m,TB}^Q$  based on the LMMSE detector.

 TABLE I  
 SIMULATION PARAMETERS

| Item                    | Value                         |
|-------------------------|-------------------------------|
| MIMO configuration      | $(N, M) = (64, 16)$           |
| Center frequency        | 4.7 GHz                       |
| Bandwidth               | 100 MHz                       |
| Subcarrier spacing      | 30 kHz                        |
| Number of subcarriers   | 192                           |
| Number of FFT point     | 256                           |
| Delay spread            | 100 ns                        |
| Delay profile           | CDL-B [54]                    |
| Channel estimation      | Perfect                       |
| Modulation scheme       | Gray-coded 4QAM, 16QAM, 64QAM |
| Channel coding scheme   | LDPC [21]                     |
| Number of EP iterations | $T = 8$                       |
| Damping Parameter       | $\alpha = 0.5$                |

these LLRs and determine the output BLER by running the channel decoder.

5) Curve Construction: Repeat over a range of input MIs to obtain the complete EXIT curve.

By precomputing EXIT curves for all MCS indices in the

5G NR-compliant MCS table, the post-decoding BLER for each MCS can be predicted directly from the demodulator output MI—eliminating the need for the actual decoding process. These curves are generated to reflect the statistical properties of the LLRs in practical higher-order modulations.

Fig. 5 shows the resulting EXIT curves, illustrating the relationship between the decoder input MI  $I_{TB}$  and the post-decoding BLER for each MCS index. The MCS table follows the 5G NR specification [55] and defines 28 MCS indices, grouped by modulation scheme: 4QAM (indices 0–9), 16QAM (indices 10–16), and 64QAM (indices 17 to 27). Low-density parity-check (LDPC) codes [21] are used for channel coding. As the MCS index increases, the corresponding code rate—and thus the data rate—also increases. Figs. 5 (a)–(c) correspond to 4QAM, 16QAM, and 64QAM, respectively.

### C. MCS Index Selection

Given the predicted post-MUD MI  $\tilde{I}_{m,TB}^Q$  in (6) for  $Q \in \{4, 16, 64\}$ , the highest MCS index  $\{\xi_m^4, \xi_m^{16}, \xi_m^{64}\}$  that satisfies the reference BLER is selected for each UE using the

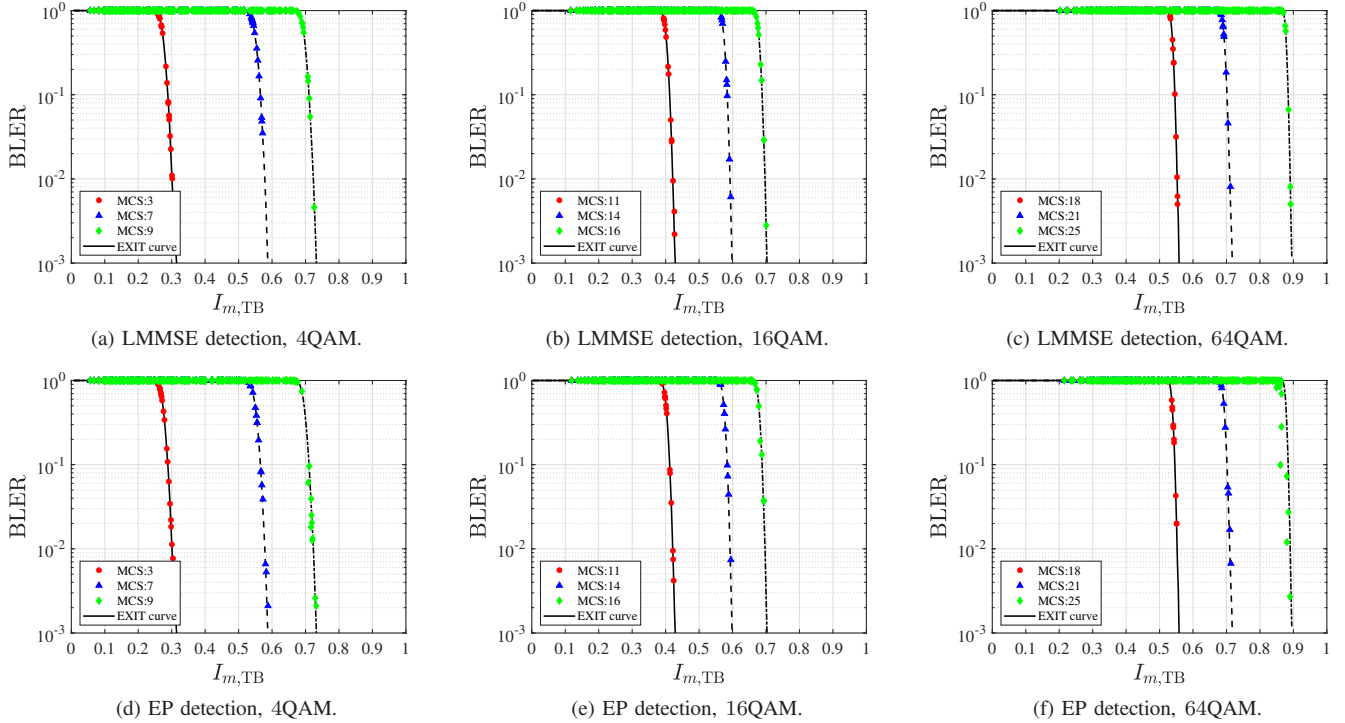


Fig. 7. Scatter plots of decoder input MI  $I_{m,TB}$  versus BLER.

EXIT curves in Fig. 5. The final MCS index  $\xi_m$  assigned to each UE is then determined as the maximum among these candidates:

$$\xi_m = \max(\xi_m^4, \xi_m^{16}, \xi_m^{64}). \quad (7)$$

This procedure underscores that in MI-based MCS selection, accurate prediction of the post-MUD MI is essential for achieving optimal performance.

#### D. Evaluation of Post-MUD MI Prediction

Computer simulations were performed to evaluate the accuracy of the post-MUD MI predicted by (6) for the LMMSE filtering in a massive MU-MIMO-OFDM system. The simulation parameters are summarized in Tab. I. Sixteen synchronized UEs ( $M = 16$ ), each with a single TX antenna, simultaneously transmit to a BS equipped with  $N = 64$  RX antennas. The 3rd generation partnership project (3GPP) clustered delay line (CDL) channel model [54] is employed. The carrier frequency is 4.7 GHz, the system bandwidth is 100 MHz, and the OFDM subcarrier spacing is 30 kHz. We consider one time-slot OFDM transmission over  $L = 192$  subcarriers (16 RBs) with an fast Fourier transform (FFT) size of 256. The number of coded bits per TB is  $N_{TB} = R \times L \times S = 2688S$ . The demodulator output MI is computed from (4) for each  $N_{TB}$ -bit codeword. To isolate prediction accuracy, all UEs are assumed to use the same modulation scheme ( $Q \in \{4, 16, 64\}$ ), and the average received SNR  $\rho$  is varied from  $-10$  dB to 24 dB in 0.5 dB increments.

Fig. 6 shows scatter plots of the measured MI  $I_{m,TB}$  from (4) (vertical axis) versus the predicted MI  $\tilde{I}_{m,TB}^Q$  from (6) (horizontal axis). The solid black line represents the ideal case ( $I_{m,TB} = \tilde{I}_{m,TB}^Q$ ), indicating perfect prediction, while the dashed lines ( $I_{m,TB} = \tilde{I}_{m,TB}^Q \pm 0.05$ ), denote a reference prediction error (PE) of 0.05. Figs. 6(a)-(c) present results

for LMMSE-based MUD across all modulation schemes. As expected, the measured samples (red dots) lie closely along the ideal line, confirming the high accuracy of the analytical MI prediction. This validates the accuracy of the prediction procedure described in Subsection III-A.

Next, we investigate the deviation observed when the actual MUD employs EP-based iterative detection, compared with predictions assuming LMMSE-based MUD. As shown in Figs. 6(d)-(f) for EP-based MUD ( $T = 8$  in Algorithm 1), most samples lie above the ideal line due to the iterative gain in MI over the LMMSE-based prediction.

These results indicate that using (6) for MCS selection together with EP-based MUD can provide highly reliable communication while substantially reducing retransmissions, and further suggest that if MI prediction tailored for EP-based MUD could achieve accuracy comparable to that for LMMSE-based MUD, additional throughput gains could be realized through better-aligned MCS selection.

#### E. Evaluation of Post-Decoding BLER Prediction

Finally, using the same simulation settings as in the previous subsection, we evaluate the accuracy of converting post-MUD MI to post-decoding BLER via the EXIT curves in Fig. 5. Fig. 7 shows BLER versus the measured MI  $I_{m,TB}$  from (4), with the aim of isolating the EXIT-curve-based conversion accuracy; thus, predicted MI is not used in this evaluation. The black curves are the EXIT curves for the selected MCS indices, directly taken from Fig. 5, while the scatter plots represent (post-MUD MI, post-decoding BLER) pairs measured in actual MU-MIMO-OFDM transmission. For each modulation scheme, three MCS indices from the 5G NR MCS table [55] are tested. Figs. 7 (a)-(c) present results with LMMSE-based MUD ( $T = 1$  in Algorithm 1), and Figs. 7 (d)-(f) with EP-based MUD ( $T = 8$ ).

In both cases, the measured samples align closely with the EXIT curves, confirming that even with nonlinear iterative detection, each stream after MUD behaves equivalently to an AWGN channel and that the designed EXIT curves accurately characterize the relationship between decoder input (*i.e.*, post-MUD) MI and post-decoding BLER. This validates the accurate modeling of the decoding characteristics described in Subsection III-B. Therefore, the EXIT curves in Fig. 5 can serve as conversion functions from predicted post-MUD MI  $\tilde{I}_{m, \text{TB}}$  to predicted BLER. By preparing EXIT curves for each code length in advance, the predicted post-MUD MI can be directly mapped to the expected post-decoding BLER for any MCS index.

The above findings indicate that realizing the system throughput gains offered by advanced iterative MUD requires accurate prediction of the enhanced post-MUD MI observed in Figs. 6 (d)–(f). In the next section, we present a prediction method specifically designed to capture this improvement.

#### IV. PROPOSED VSS-BASED MI PREDICTION

Fig. 8 illustrates the proposed VSS-based MI prediction framework employing ANN search over a VDB, which comprises two phases: (a) an offline VDB construction phase and (b) an online MI prediction phase. In the offline phase (a), a feature vector (key) is generated from the CSI  $\mathbf{H}$  and the average received SNR  $\rho$  and is paired with the measured MI (value) obtained from MU-MIMO-OFDM transmission over the corresponding wireless channel when detection is performed using the EP-based MUD. These key–value pairs are stored in the VDB in vector format. This process is typically performed offline—either through simulations or measurements in real environments—but can also be executed online, with the VDB being incrementally updated as new measurement data becomes available.

In the online phase (b), a key is generated in the same manner from the estimated CSI and average received SNR. An ANN search is then conducted on the VDB to retrieve a specified number of nearest-neighbor keys, and the associated values are returned. These values correspond to MIs achieved under similar channel conditions; thus, with an appropriately designed feature vector, highly accurate MI predictions can be achieved. In this study, the Faiss library [35] is adopted for ANN search due to its efficient GPU-based implementation. The detailed procedures for both phases are described in the following subsections.

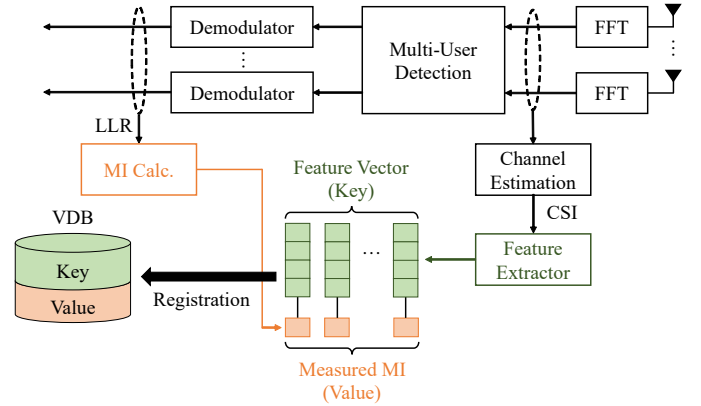
##### A. Offline VDB Construction Phase

The VDB contains  $D_{\text{VDB}}$  entries, each comprising a feature vector (key)  $\mathbf{v} \in \mathbb{R}^{D_{\text{key}} \times 1}$  and its associated acquired knowledge (value)  $\varepsilon \in \mathbb{R}$ , stored as a pair  $(\mathbf{v}, \varepsilon)$ . In this study, keys are extracted from the CSI  $\mathbf{H} \in \mathbb{C}^{N \times M \times L}$  and the average received SNR  $\rho \in \mathbb{R}$  via the feature extraction function:

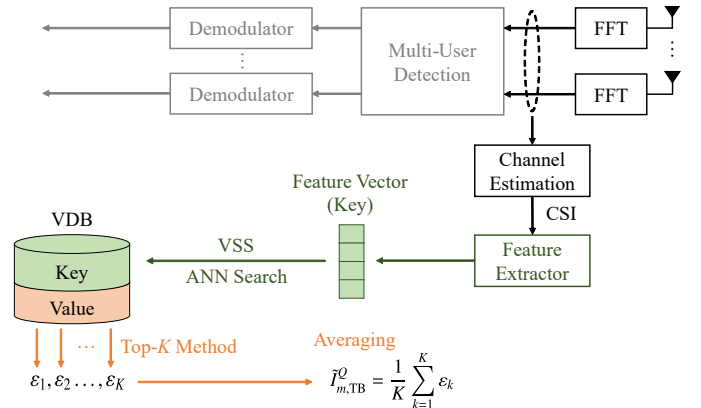
$$\mathbf{v} = f(\mathbf{H}, \rho), \quad (8)$$

whose design critically influences prediction accuracy.

Since MCS selection requires MI prediction on a per-UE basis, feature vectors are computed individually for each UE, with  $\mathbf{v}_m \in \mathbb{R}^{D_{\text{key}} \times 1}$  denoting the vector for the  $m$ -th UE, as illustrated in Fig. 8 (a). The values  $\varepsilon$  correspond to the measured demodulator output (post-MUD) MI  $I_{m, \text{TB}}$  in



(a) Offline VDB construction phase.



(b) Online MI prediction phase.

Fig. 8. Block diagram of MI prediction using the VDB and VSS.

(4), obtained from the LLRs computed after actual OFDM transmission over wireless channel  $\mathbf{H}$  and subsequent MUD. A large set of channel realizations is generated according to a stochastic channel model, and all resulting  $(\mathbf{v}_m, I_{m, \text{TB}})$  pairs are stored in the VDB for later ANN-based retrieval.

##### B. Online MI Prediction Phase

The first task is to compute the feature vector corresponding to the current channel state, following the same procedure as in the offline phase. Let the estimated CSI and average received SNR be denoted by  $\hat{\mathbf{H}} \in \mathbb{C}^{N \times M \times L}$  and  $\hat{\rho} \in \mathbb{R}$ , respectively. The key for the  $m$ -th UE is then generated using (8) as

$$\hat{\mathbf{v}}_m = f(\hat{\mathbf{H}}, \hat{\rho}), \quad (9)$$

and used as a query vector for ANN search on the VDB.

In the GPU-based implementation, the Faiss library [35] employs two key techniques to enable large-scale, low-latency VSS. The first is inverted file (IVF) indexing [56], which partitions the database into  $K_{\text{IVF}}$  clusters using k-means clustering and stores only the representative vector (*centroid*) of each cluster, with each data point associated with its corresponding centroid. The second is product quantization (PQ) [57], which decomposes each  $D_{\text{key}}$ -dimensional key into  $D_{\text{sub}}$ -dimensional sub-vectors, each independently quantized. As a result, each data point is stored as a quantization code, eliminating the need to store the original high-dimensional vector. This approach significantly reduces the memory footprint of

the VDB and enables fast distance computation through the use of lookup tables. During an ANN search, Faiss first performs a nearest-neighbor search among the centroids and selects the  $P_{\text{IVF}}$  clusters, including the cluster whose centroid has the highest similarity to the query vector and its neighboring clusters. A similarity search is subsequently conducted only within the selected clusters to retrieve the approximate nearest neighbor. This approach avoids an exhaustive search across all data points and significantly reduces the search space by focusing only on data points that are likely to be close to the query vector. The parameter  $P_{\text{IVF}}$  governs the trade-off between search accuracy and computational complexity, enabling efficient retrieval with low memory usage even for large-scale VDB.

The cost of the VSS is evaluated in terms of the number of search operations  $N_s$ . In an exhaustive nearest-neighbor search, referred to as the Flat index in the Faiss library, the number of search operations  $N_s$  for a single query vector is equal to the VDB size and thus scales on the order of  $N_s$ . In contrast, for the IVFPQ index, which combines an IVF index with PQ,  $N_s$  grows on the order of

$$\mathcal{O} \left( K_{\text{IVF}} + P_{\text{IVF}} \times \frac{D_{\text{VDB}}}{K_{\text{IVF}}} \right). \quad (10)$$

The first term in (10) represents the number of distance computations required for the nearest-centroid search, whereas the second term corresponds to the number of distance computations for data points within the selected clusters. From (10),  $N_s$  is minimized when  $K_{\text{IVF}} = \sqrt{P_{\text{IVF}} D_{\text{VDB}}}$ . In this study, based on the guidelines provided in the official documentation [35] as well as empirical experiments from practical use, we adopt  $K_{\text{IVF}} = 4\sqrt{D_{\text{VDB}}}$  as a setting that achieves a favorable balance between computational efficiency and search accuracy. By appropriately adjusting  $K_{\text{IVF}}$ , the search complexity  $N_s$  can be controlled to scale at most as  $\mathcal{O}(\sqrt{D_{\text{VDB}}})$ , thereby ensuring both efficiency and scalability.

Although it is possible to directly use the value returned by the ANN search with the key  $\hat{v}_m$  generated in (9) as the predicted MI, the inherent approximation in the ANN search does not guarantee retrieval of the exact nearest neighbor. Moreover, depending on the design of the feature vectors and the scale of the VDB, the value associated with the nearest key may not necessarily yield the optimal MI prediction. To improve the robustness of the prediction, we also employ the Top- $K$  method for the ANN output [38]. Specifically, as illustrated in Fig. 8 (b), during the ANN search, we extract the values associated with the top  $K$  keys that yield the highest approximate vector similarity computed internally, and then use their average as the final MI prediction, as given by

$$\tilde{I}_{m,\text{TB}}^Q = \frac{1}{K} \sum_{k=1}^K \varepsilon_k, \quad (11)$$

where  $\varepsilon_1, \dots, \varepsilon_K$  are the values associated with the top  $K$  keys. The pseudocode of the VSS-based MI prediction using the Top- $K$  method is presented in Algorithm 2.

### C. Design of Feature Vector

A feature vector is a low-dimensional representation that robustly and sufficiently extracts the information required for the target task from an extremely high-dimensional parameter

---

### Algorithm 2 VSS-based MI prediction using Top- $K$ method

---

**Require:** Estimated CSI  $\hat{H}$ , average SNR  $\hat{\rho}$ ,  
VDB for  $Q$ -QAM  
**Ensure:** Predicted MI  $\tilde{I}_{m,\text{TB}}^Q$

---

- 1: Compute the feature vector (key):  $\hat{v} = f(\hat{H}, \hat{\rho})$
  - 2: Execute Top- $K$  ANN search using query  $\hat{v}$
  - 3: Obtain top  $K$  pairs in descending order of similarity:  $(\mathbf{v}_1, \varepsilon_1), (\mathbf{v}_2, \varepsilon_2), \dots, (\mathbf{v}_K, \varepsilon_K)$
  - 4: Compute the average:  $\tilde{I}_{m,\text{TB}}^Q = \frac{1}{K} \sum_{k=1}^K \varepsilon_k$
- 

space characterizing the wireless environment. In other words, its design is the key factor that determines the success or failure of the proposed approach. Meanwhile, although wireless channels vary according to stochastic events, their variations exhibit strong correlations across the time, frequency, and spatial domains. By designing a feature vector that effectively captures these characteristics, it becomes possible to achieve accurate predictions with a much smaller database size than that required for other applications, such as natural language processing and high-dimensional image classification.

The fundamental principle of feature vector design in this study is that, within the limits of practical feasibility, one should identify a low-dimensional representation that can analytically explain the target task, relying as much as possible on a mathematical approach. In Section III, we demonstrated that the demodulator output MI after LMMSE detection can be analytically estimated on a TB-wise basis. On the other hand, analytically predicting the convergence behavior of EP is intrinsically difficult. Therefore, the demodulator output MI after LMMSE detection, which corresponds to the first iteration of EP, is positioned as a limiting metric that can analytically explain the target task of predicting the demodulator output MI after EP detection.

Based on the above discussion, we construct the feature vector in this paper using the predicted MI obtained with LMMSE-based MUD for each subcarrier, *i.e.*,  $\tilde{I}_m^Q[\ell]$  in (6). Considering all  $L = 192$  subcarriers that constitute one TB, the feature vector is given by<sup>3</sup>

$$\mathbf{v}_m = [\tilde{I}_m^Q[1], \tilde{I}_m^Q[2], \dots, \tilde{I}_m^Q[192]]^T \in \mathbb{R}^{192 \times 1}, \quad (12)$$

where the ANN search over the VDB can be interpreted as transforming the per-subcarrier MI obtained with LMMSE-based MUD into the TB-wise MI with EP-based MUD.

### D. Evaluation of MI Prediction Accuracy

Computer simulations were conducted to evaluate the prediction accuracy achieved with the feature vector defined in (12). The simulation conditions were identical to those in Subsection III-E, *i.e.*, the parameters listed in Tab. I. The VDB size was fixed at  $D_{\text{VDB}}$  for all modulation schemes, and the data points (220800), corresponding to 200 channels, were used for accuracy evaluation. The channel realizations for evaluation were generated independently from those used

<sup>3</sup>In fact, through a preliminary ablation study, we have confirmed that this mathematically grounded feature vector achieves clearly superior performance compared with other conceivable alternative designs.

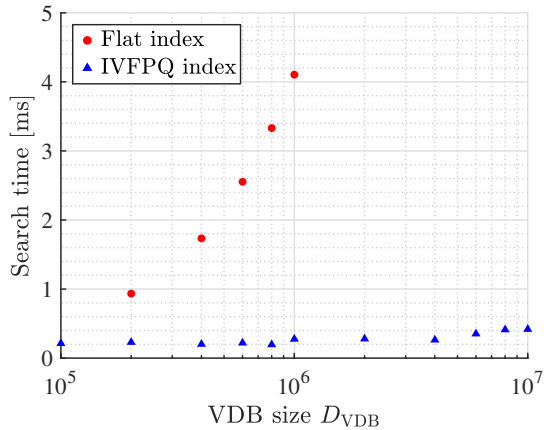


Fig. 9. Search time versus VDB size under a worst-case evaluation scenario, where the VDB stores 192-dimensional real-valued feature vectors with independently and uniformly distributed elements in the range  $[0, 1]$ .

for offline VDB construction. The average received SNR was varied from  $-10$  dB to  $24$  dB in  $0.5$  dB increments. Consequently, the VDB size is given by the product of the number of channel realizations, the number of SNR points, and the number of UEs. The internal ANN search parameters were set to  $(K_{\text{IVF}}, D_{\text{sub}}, P_{\text{IVF}}) = (4\sqrt{D_{\text{VDB}}}, 12, 10)$ ,

First, to demonstrate the practical feasibility of the proposed method, we evaluate the online search latency of VSS implemented on a GPU using the Faiss library. Although the processing latency in practical deployments depends on the system configuration and execution conditions, all simulation results presented in this paper were obtained on a commercially available personal computer equipped with an NVIDIA GeForce RTX 4070 SUPER GPU.

Fig. 9 shows the search time as a function of the VDB size  $D_{\text{VDB}}$  for each index type, namely, the Flat index and the IVFPQ index. The horizontal axis represents  $D_{\text{VDB}}$ , while the vertical axis shows the search time per query vector. For the Flat index, since distance computations are required for all data points, the search time increases rapidly in proportion to the VDB size. In contrast, for the IVFPQ index (*i.e.*, ANN search), the search time remains almost constant even as the VDB size increases. This behavior arises because the search is restricted to a small number of clusters in the vicinity of the query vector, indicating that an increase in the VDB size has little impact on the actual number of candidate points examined during the search. Although the required VDB size is discussed later, these results indicate that, with fast ANN-based VSS, the search time can be reduced to the order of several hundred microseconds even on a commercially available GPU. Moreover, owing to its high scalability, we conclude that the VSS search time does not constitute a dominant computational bottleneck in the proposed method.

In the following, we first evaluate the variation in prediction accuracy and robustness with respect to the VDB size and the Top- $K$  parameter. Based on these results, we then assess the MI prediction accuracy of the proposed method using the selected parameter settings.

1) *Impact of the VDB Size*: Fig. 10 illustrates the variation in prediction accuracy as a function of the VDB scale. The horizontal axis represents the number of user channel realizations for each average received SNR, which determines

the database scale and is proportional to the VDB size. The vertical axis shows the probability that the prediction error, defined as  $\tilde{I}_{m,\text{TB}}^Q - I_{m,\text{TB}}$ , falls within the ranges of  $\pm 0.01$ ,  $\pm 0.02$ , and  $\pm 0.05$ . The Top- $K$  parameter is set to  $K = 1, 5$ , and  $20$ , respectively.

From the results, it can be observed that, for all modulation schemes, once the number of user channel realizations exceeds approximately  $3,200$  (*i.e.*,  $200$  channel realizations  $\times$   $16$  UEs), the prediction accuracy becomes almost insensitive to further increases in the VDB scale. This indicates that approximately  $3,200$  user channel realizations are sufficient to capture the statistical characteristics of the CDL-B channel model compliant with the 5G NR specification that are required to accomplish the target task of predicting the demodulator output MI after EP detection. At the same time, this observation suggests that the effectiveness of the proposed approach strongly depends on the appropriately designed feature vector. Furthermore, these findings not only indicate that offline VDB construction does not incur excessive computational costs but also suggest the feasibility of online VDB updates.

2) *Impact of the Top- $K$  Parameter*: Next, based on the results of the previous experiments, we evaluate the impact of the Top- $K$  parameter on the prediction accuracy by fixing the number of user channel realizations per average received SNR to  $3,200$ . Fig. 11 illustrates the variation in prediction accuracy as a function of the Top- $K$  parameter. The horizontal axis represents the number of samples  $K$  used for averaging in the Top- $K$  method, while the vertical axis shows, as in Fig. 10, the probability that the prediction error falls within a prescribed range.

From Fig. 11, it can be observed that, for all modulation schemes, the prediction accuracy improves monotonically as the averaging parameter  $K$  increases. This is because the candidates returned by the ANN search are approximate rather than exact nearest neighbors. When only a single search result is used, the approximation error inherent in ANN search can degrade prediction accuracy. In contrast, averaging the prediction values obtained from multiple ANN outputs effectively generalizes the estimation and mitigates the impact of approximation errors. Although increasing  $K$  enlarges the scale of parallel searches, values of  $K$  on the order of several tens—sufficient to achieve adequate generalization performance—do not pose practical computational burdens even on commercially available GPUs. Furthermore, as expected, the improvement in prediction accuracy exhibits diminishing returns as  $K$  becomes sufficiently large and eventually saturates. Under the experimental conditions considered in this study, we confirmed that  $K = 20$  provides a favorable trade-off between prediction accuracy and the degree of parallel search.

3) *MI Prediction Accuracy*: Based on the above results, we set the parameters accordingly and evaluate the MI prediction accuracy. A total of  $400$  MU-MIMO-OFDM channel realizations satisfying the parameter settings in Tab. I were generated, of which  $200$  were used for VDB construction and the remaining  $200$  for evaluation. In this setup, the VDB size is given by the product of the number of channel realizations, the number of UEs, and the number of SNR points, *i.e.*,  $D_{\text{VDB}} = 200 \times 16 \times 69 = 220800$ . The internal ANN search parameters are set to  $(K_{\text{IVF}}, D_{\text{sub}}, P_{\text{IVF}}) = (1879, 12, 10)$ , and the Top- $K$  parameter is set to  $K = 20$ .

Fig. 12 shows scatter plots of the predicted and measured

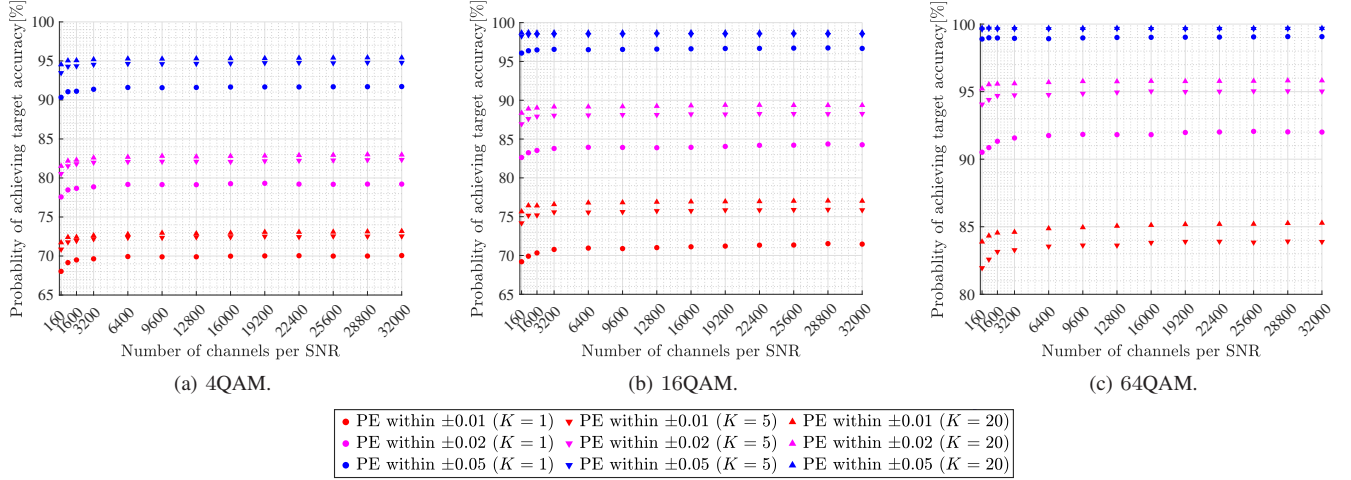


Fig. 10. Prediction performance versus VDB size, evaluated by the probability that the MI prediction error falls within specified bounds.

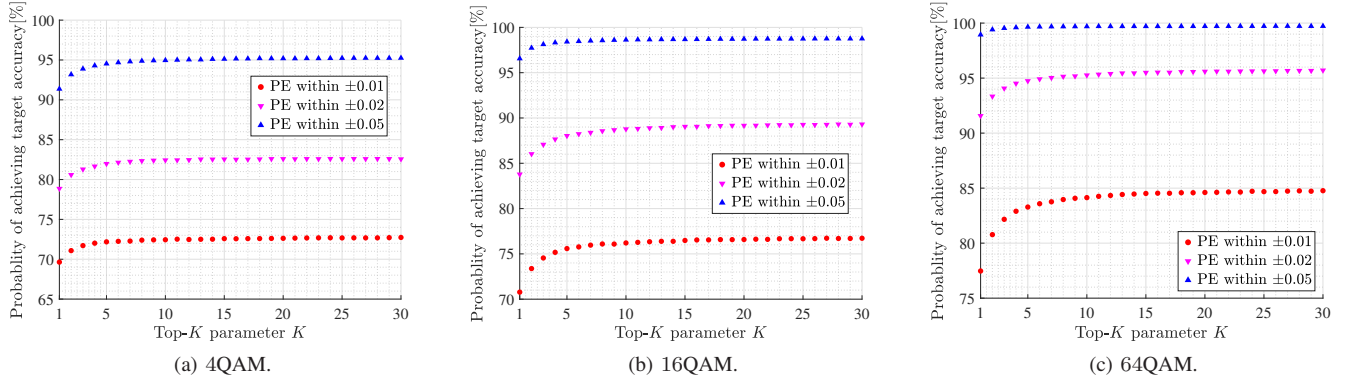


Fig. 11. Prediction performance versus Top-K parameter, evaluated by the probability that the MI prediction error falls within specified bounds.

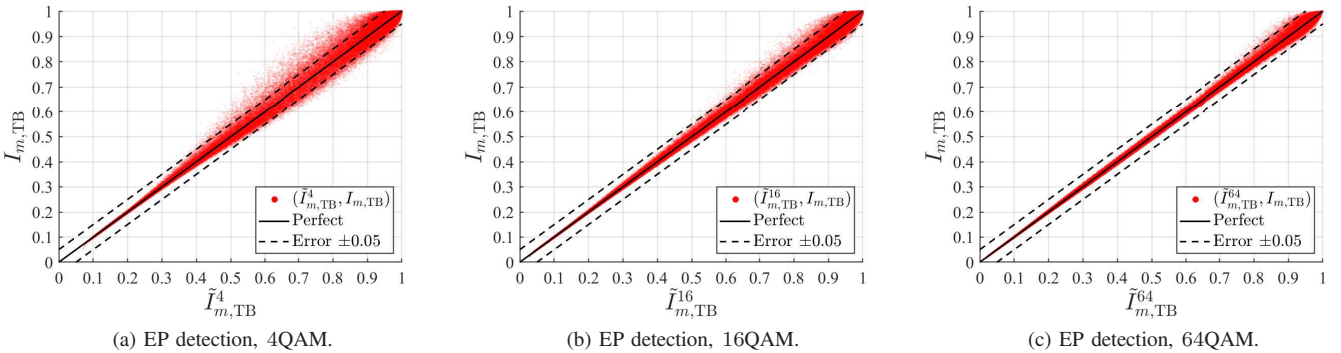

 Fig. 12. Scatter plots of the measured MI  $I_{m,TB}$  versus the predicted MI  $\tilde{I}_{m,TB}^Q$  based on the proposed method.

 TABLE II  
 PREDICTION ACCURACY

| Modulation scheme | 4QAM     | 16QAM    | 64QAM     |
|-------------------|----------|----------|-----------|
| PE within ±0.01   | 72.61%   | 76.57%   | 84.67%    |
| PE within ±0.02   | 82.60%   | 89.13%   | 95.64%    |
| PE within ±0.05   | 95.21%   | 98.73%   | 99.70%    |
| PE over +0.01     | 12.23%   | 11.17%   | 7.66%     |
| PE over +0.02     | 7.47%    | 4.67%    | 1.71%     |
| PE over +0.05     | 1.27%    | 0.12%    | 0.014%    |
| MSE               | 0.000462 | 0.000185 | 0.0000676 |

MI pairs  $(\tilde{I}_{m,TB}^Q, I_{m,TB})$  in the same manner as Fig. 6. Tab. II summarizes the percentage of samples with a PE

within  $\pm 0.01$ ,  $\pm 0.02$ , and  $\pm 0.05$ ; the percentage exceeding the measured values by more than  $+0.01$ ,  $+0.02$ , and  $+0.05$ ; and the MSE between the predicted and measured MIs. From Fig. 12, the sample points are concentrated near the ideal prediction line  $I_{m,TB} = \tilde{I}_{m,TB}^Q$ , and their variance decreases as the modulation order increases. From the numerical results in Tab. II, for all modulation schemes, more than 95% of the samples have a PE within  $\pm 0.05$ , and more than 70% are within  $\pm 0.01$ . Since a PE exceeding 0.05 could lead to selecting an adjacent MCS index, this accuracy can be considered sufficient for the intended purpose. Furthermore, the percentage of MI overestimations relative to the measured

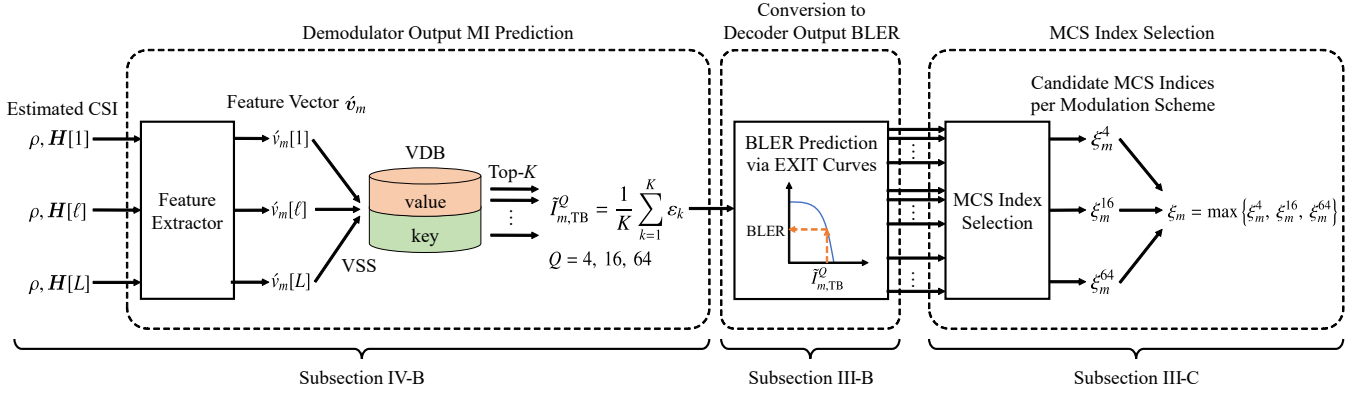


Fig. 13. Block diagram of the proposed MI-based MCS selection process incorporating the VSS-based MI prediction method.

values—which could increase the BLER—is less than 2% for a PE threshold of 0.05 (i.e.,  $\tilde{I}_{m,\text{TB}}^Q \geq I_{m,\text{TB}} + 0.05$ ), and is even smaller for higher-order modulation schemes, where such errors are more critical. These results demonstrate that the proposed method, using (12) as the key, can predict the post-MUD MI for EP-based MUD with sufficient accuracy to enable appropriate MCS index selection.

## V. THROUGHPUT EVALUATION

Finally, the effectiveness of the proposed MCS selection framework is validated from a throughput perspective.

### A. Proposed VSS-aided MCS Selection Framework

Fig. 13 illustrates the overall workflow of the MCS selection process incorporating the proposed VSS-based MI prediction scheme, corresponding to Fig. 2 in Section III. Note that the demodulator output (post-MUD) MI prediction block in Fig. 2 is replaced with the proposed method described in Section IV. The key advantage of the proposed framework is its applicability to *any* MUD scheme whose decoder input cannot be derived analytically. As a representative example, this paper investigates EP-based MUD, well known for its high detection accuracy, and verifies whether its performance gains can be translated into throughput improvements.

### B. Throughput Evaluation

The simulation conditions are identical to those in Section III, as listed in Tab. I, and the VDB used for MI prediction is the same as in Section IV. The MCS table follows the 5G NR standard [55], enabling BLER prediction using the EXIT curves shown in Fig. 5 in Subsection III-B. The reference BLER for MCS selection is set to 0.001<sup>4</sup>. For system performance evaluation, 200 independently generated channels are used. These channels are identical to those used for evaluating MI prediction accuracy in Subsection IV-D. Throughput is calculated by performing OFDM transmission over  $N_{\text{slot}}$  time slots. Small-scale fading varies across slots, and MCS selection is updated every 20 slots,<sup>5</sup> corresponding to one frame [48]. The user throughput is calculated as the

<sup>4</sup>While a reference BLER of 0.1 is commonly adopted in practice [58], [59], this study employs a more stringent value to ensure highly reliable transmission with advanced detectors. This also mitigates the risk of throughput degradation due to overestimation of channel quality.

<sup>5</sup>According to the 5G NR standard [48], when the subcarrier spacing is 30 kHz, one frame consists of two subframes, each containing 10 time slots.

sum of bits successfully transmitted without error per TB in each time slot by each UE, as follows:

$$\tau_{\text{user},m} \triangleq \frac{\sum_{n_{\text{slot}}=1}^{N_{\text{slot}}} N_{\text{sucbit},m}(n_{\text{slot}})}{N_{\text{slot}} \cdot T_{\text{slot}}} \quad [\text{Mbps}], \quad (13)$$

where  $N_{\text{sucbit},m}(n_{\text{slot}})$  [Mbit] is the number of information bits transmitted by the  $m$ -th UE in time slot  $n_{\text{slot}}$  and successfully received, counted only when the entire TB is error-free. The slot duration  $T_{\text{slot}}$  is set to  $0.5 \times 10^{-3}$  s, based on the 5G NR specification with a 30 kHz subcarrier spacing [48]. The system throughput is calculated from the total number of successfully transmitted bits across all UEs as follows:

$$\begin{aligned} \tau_{\text{sys}} &\triangleq \sum_{m=1}^M \tau_{\text{user},m} \\ &= \frac{\sum_{m=1}^M \sum_{n_{\text{slot}}=1}^{N_{\text{slot}}} N_{\text{sucbit},m}(n_{\text{slot}})}{N_{\text{slot}} \cdot T_{\text{slot}}} \quad [\text{Mbps}]. \end{aligned} \quad (14)$$

Fig. 14 shows the cumulative distribution function (CDF) of system throughput for average received SNR values of 4, 12, and 20 dB. The following methods for predicting the post-MUD MI are compared, where (\*) specifies the detector employed as the MUD (either LMMSE or EP):

- ZF-based SINR (\*): This scheme assumes equalization based on the least square (LS) criterion and predicts the MI using the effective SINR of each subcarrier [14], [15]. It is a well-known prediction approach employed in the classical MCS selection framework and serves as a reference to evaluate the effectiveness of the proposed scheme. This approach is equivalent to using a ZF detector as the MUD, in which case the post-MUD SINR is analytically computed in closed form from the CSI and the average received SNR as

$$\gamma_{m,\text{ZF}}[\ell] = \rho \cdot \frac{1}{\left[ (\mathbf{H}^H[\ell] \mathbf{H}[\ell])^{-1} \right]_{m,m}}. \quad (15)$$

For the TB-level channel quality metric, the average effective SINR is used. This is obtained by converting the computed per-subcarrier effective SINR values into transmission rates based on Shannon capacity, averaging them over all subcarriers, and then converting the result back into effective SINR:

$$\bar{\gamma}_{m,\text{ZF}} = \phi^{-1}(\bar{R}_m), \quad (16a)$$

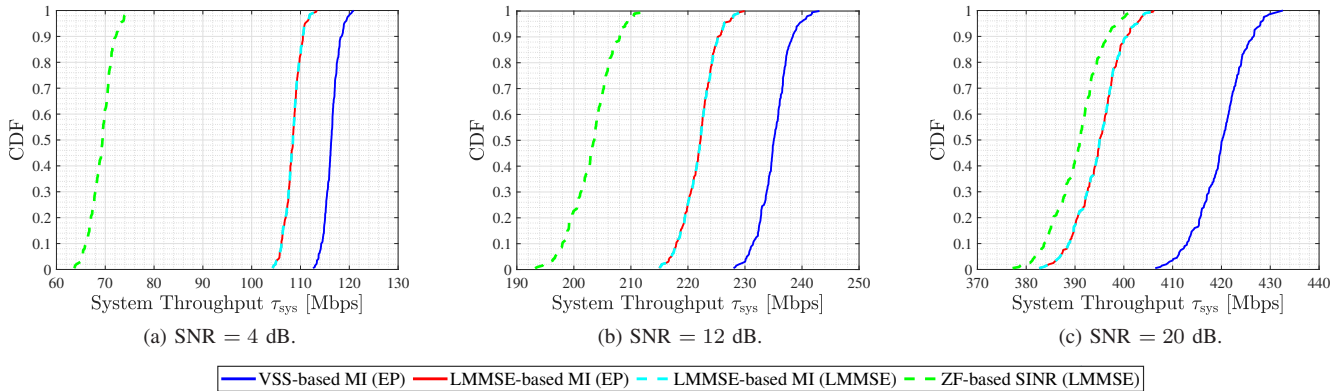


Fig. 14. System throughput performance for various average received SNR levels in an MU-MIMO-OFDM system.

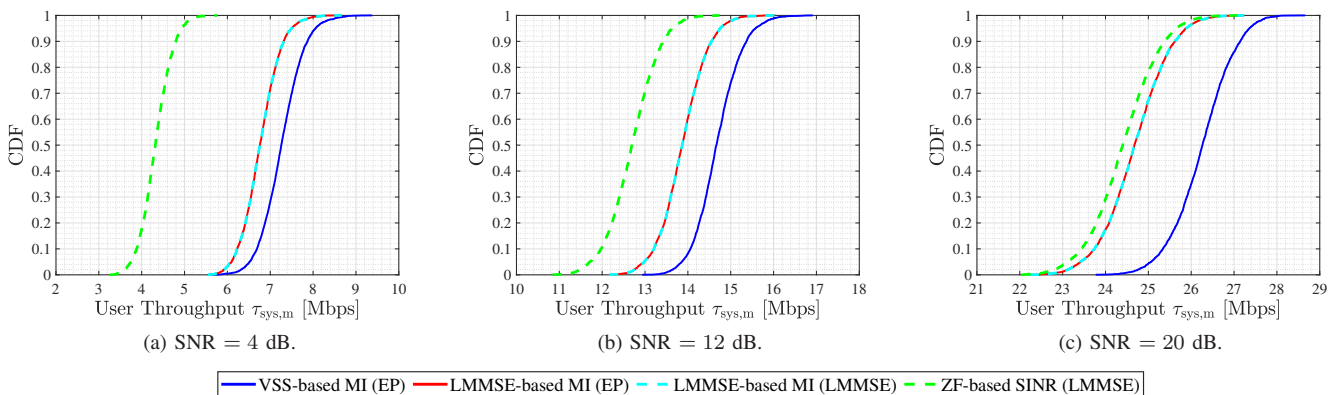


Fig. 15. User throughput performance for various average received SNR levels in an MU-MIMO-OFDM system.

$$\bar{R}_m = \frac{1}{L} \sum_{\ell=1}^L \phi(\gamma_{m,\text{ZF}}[\ell]), \quad (16b)$$

where  $\phi(x) \triangleq \log_2(1+x)$ . MCS selection is then performed by mapping the average SINR in (16) to BLER using the SNR–BLER characteristics of an AWGN channel, and selecting, for each UE, the highest MCS index that satisfies the reference BLER [14], [15].

- LMMSE-based MI (\*): This scheme employs the MI-based MCS selection framework described in Section III, with the workflow diagram shown in Fig. 2. The MI prediction method in (6) is adopted [23], where the prediction accuracy of the post-MUD MI corresponds to Fig. 6, and its mapping to post-decoding BLER corresponds to Fig. 7.
- VSS-based MI (\*): This scheme incorporates the VSS-based MI prediction described in Section IV, with the workflow diagram shown in Fig. 13. Post-MUD MI prediction is performed using the VDB and ANN, where the prediction accuracy of the post-MUD MI corresponds to Fig. 12, and its mapping to post-decoding BLER corresponds to Fig. 7 (d)–(f).

We examine the results in Fig. 14. First, for the ZF-based SINR scheme [15], the system throughput markedly degrades, especially in the low-SNR regime. There are two causes: (i) reduced accuracy of post-MUD MI prediction due to the detection-performance gap between the LMMSE and ZF detectors, and (ii) BLER-mapping error introduced by the

averaging operation via Shannon capacity, which is not aligned with transmission using discrete constellations. Consequently, although this framework is widely adopted regardless of the underlying MUD, it often fails to assign an appropriate MCS in practice. Many practical systems gradually mitigate this issue using correction mechanisms such as OLLA [15], [58]–[60]; however, the throughput during the initial phase of link adaptation tends to be significantly reduced. These results also suggest that when OLLA underperforms, or in mission-critical communications, the conventional approach may fail to ensure highly reliable communication. Next, with the LMMSE-based MI scheme (LMMSE), substantial throughput gains are observed over the conventional ZF-based method, despite using the same MUD. This improvement stems from analytical post-MUD MI prediction and accurate mapping to post-decoding BLER via EXIT curves, which enable proper MCS selection. Specifically, the average throughput improves by approximately (a) 40 Mbps at 4 dB, (b) 20 Mbps at 12 dB, and (c) 5 Mbps at 20 dB. The smaller gain at high SNR arises because the performance gap between the LMMSE and ZF detectors narrows in this region.

The most notable observation is that changing the MUD from LMMSE to EP does not improve the system throughput when MCS selection remains based on the LMMSE criterion (*i.e.*, the LMMSE-based MI scheme with EP). This indicates that merely enhancing the detector does not translate into throughput gains unless the MCS selection strategy is co-designed with the adopted MUD.

Finally, when the EP detector is used as the MUD and the

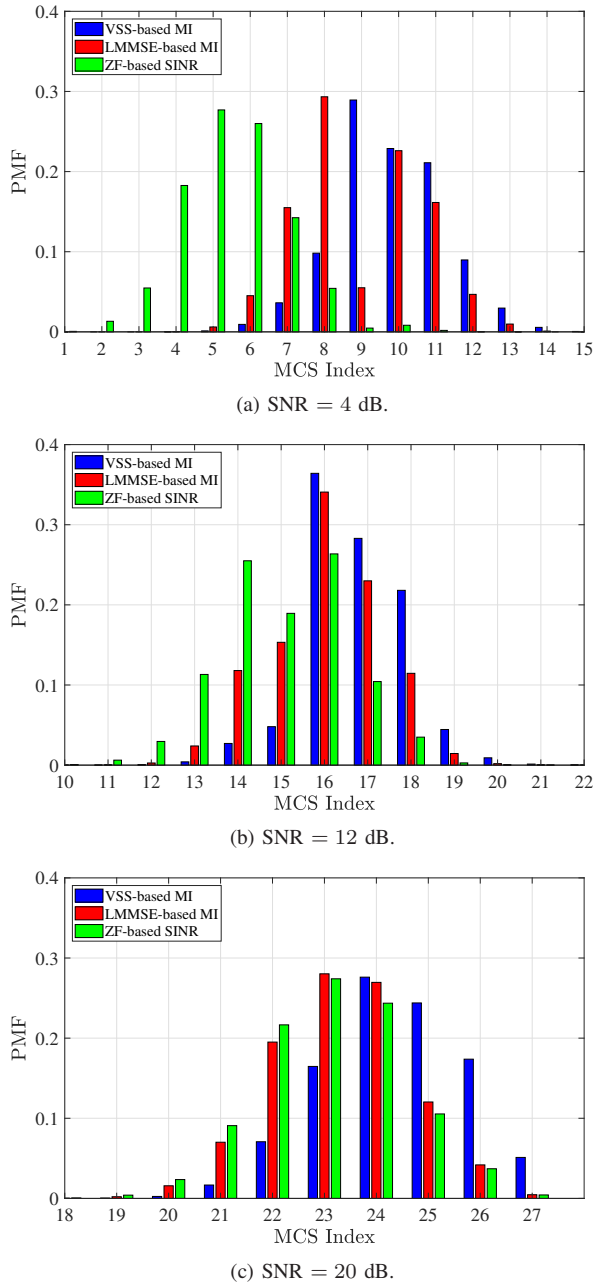


Fig. 16. PMF of MCS indices assigned to UEs.

proposed VSS-based MI prediction is incorporated into MCS selection, the system throughput improves significantly across all SNRs. Relative to the LMMSE-based MCS assignment, the average improvements are approximately (a) 10 Mbps at 4 dB, (b) 15 Mbps at 12 dB, and (c) 25 Mbps at 20 dB. These results demonstrate that the proposed framework is crucial for leveraging advanced iterative MUD in practical systems.

Fig. 15 shows the CDF of user throughput for the same simulation setup as in Fig. 14. This allows us to observe variations in throughput for individual UEs under different channel conditions, which cannot be captured when only the aggregated system throughput is considered. An important insight from these results is that the proposed scheme achieves throughput improvements across all SNR and rate regions. In other words, the proposed framework does not improve the rates of certain UEs at the expense of degrading others

but rather provides gains for all UEs. This property is highly desirable in terms of UE fairness in more realistic system-level simulations. The overall trend is consistent with the system throughput results, indicating that the proposed scheme also offers substantial performance improvements over the conventional ZF-based method from the perspective of user throughput. Moreover, the gain from using the VSS-based MI prediction is most pronounced in the high SNR region, where the iterative gain of the EP detector is significant.

Fig. 16 shows the probability mass function (PMF) of the MCS indices assigned to each UE in the above simulations. With VSS-based MI prediction, the MCS selection reflects the superior detection performance of EP-based MUD, which is especially evident for higher-order modulations where the performance gap between the LMMSE and EP detectors is large. This observation explains the throughput improvements seen in the previous results. Notably, the change in the PMF resulting from different post-MUD MI prediction methods is not merely a simple parallel shift. This fact suggests that the proposed method improves the accuracy of the predicted MI at a fundamentally different level, rather than merely applying a fixed backoff correction to the predicted values.

## VI. DISCUSSION AND FUTURE WORK

In Section V, simulation results were presented under the assumption of a long-term statistically static environment after resource allocation. To prepare for the practical use and further development of the proposed method, it is important to comprehensively evaluate its performance in more realistic system-level simulations that incorporate long-term variations in channel statistics, integration with OLLA, and scheduling mechanisms responsible for resource allocation. Prior to such system-level evaluations, this section provides supplementary discussion and insights into the feasibility of the proposed method in practical systems and the potential challenges associated with integrating these components.

### A. Long-Term Variations in Channel Statistics

In practical operation, the VDB deployed at a BS is expected to be constructed based on a combination of simulation data and real measurement data collected during a warm-up phase, thereby tailoring it to the surrounding propagation environment. As a result, the occurrence of channels that significantly deviate from those stored in the VDB is unlikely to be both random and frequent. This tendency is particularly pronounced in low-frequency bands such as sub-6 GHz, where long-term environmental variations that affect channel models generally evolve slowly. Under such conditions, the proposed framework is expected to maintain high prediction accuracy stably over extended periods of operation. This expectation is further supported by the results in Subsection IV-D, where high prediction accuracy was achieved even though the evaluation employed channel realizations that were generated independently of those used for VDB construction and included medium- and short-term channel fluctuations.

Nevertheless, it is also possible that long-term channel statistics may change significantly due to gradual or abrupt environmental variations. Even in such scenarios, the proposed method is expected to maintain relatively high prediction accuracy or to recover its accuracy within a short period

through VDB updates. This is because, as shown in Fig. 10, the proposed approach can achieve an accurate prediction with a relatively small VDB, implying that the gradual addition and updating of VDB entries enable flexible adaptation to environmental changes. Immediately after a change in channel statistics, the system performs a prediction based on the most similar entries stored in the VDB, allowing rapid adaptation even to previously unseen environments. This capability to realize such flexibility through localized database updates constitutes one of the key advantages of the VDB-based framework and represents a significant benefit over conventional learning-based approaches, which typically rely on retraining.

### B. Integration with OLLA

The proposed framework can be seamlessly integrated into system-level simulations as an inner-loop link adaptation (ILLA) mechanism and operated in conjunction with conventional OLLA. In this configuration, it improves the prediction accuracy of the demodulator output MI at periodic CSI acquisition instances and enables appropriate initial MCS selection for each UE. As a result, block error occurrences—particularly in the initial stage—can be suppressed, thereby reducing the retransmission probability and contributing not only to throughput improvement but also to more stable OLLA convergence. A particularly relevant application scenario for the proposed method is ultra-reliable low-latency communications (URLLC). In general, since target BLER values are set to be very low in high-reliability communications, the update step size of OLLA becomes extremely small, which may cause OLLA alone to fail to track channel variations adequately or even to converge [59]. Moreover, under stringent latency constraints, operating OLLA alone—while implicitly assuming the occurrence of transmission errors—is not necessarily appropriate. Under such conditions, integrating the proposed framework with OLLA as an ILLA mechanism can improve the accuracy of initial MCS selection, thereby enabling both enhanced system performance and improved stability.

On the other hand, to ensure optimal operation of this integrated scheme, careful design of OLLA-related parameters, such as the update step size and control policies for spatial multiplexing, is required. These issues constitute important directions for future research.

### C. Future Challenges and Practical Feasibility

In system-level simulations, it is necessary to account for the behavior of schedulers responsible for resource allocation across the time, frequency, and spatial domains. In such scenarios, the resources allocated to each UE dynamically vary on a per-slot basis, leading to increased diversity in the channel structures experienced by individual UEs. In particular, the combinations of spatially multiplexed UEs determined by spatial resource allocation have a significant impact on detector performance and, consequently, on communication quality assessment for rate control.

Under such scheduler-coupled environments, the design and operation of a VDB tailored to the scheduler behavior become important issues for further investigation. Specifically, this introduces new challenges, including further refinement of feature vector design, advanced VDB construction strategies (e.g., database scale, partitioning methods, and granularity design), and more sophisticated VSS processes (e.g., hierarchical

search and parameter optimization) [61]. Nevertheless, these challenges do not constitute fundamental technical barriers that undermine the practical feasibility of the proposed framework and are expected to be adequately addressed through systematic future studies.

Overall, these considerations highlight that the proposed framework provides a flexible and extensible foundation for system-level operation in scheduler-driven wireless networks.

## VII. CONCLUSION

In this paper, we proposed an MI-based MCS selection framework that incorporates a VSS-based MI prediction scheme for massive MU-MIMO-OFDM systems employing advanced MUD. The framework designs all MCS selection processing based on TB-level MI, where the mapping from high-accuracy post-MUD MI to post-decoding BLER is enabled through a prediction function tailored to the MCS table using EXIT curves. When an LMMSE detector, for which the post-MUD MI can be analytically predicted, is employed, the framework achieves optimal MCS selection with respect to the reference BLER. Furthermore, when an EP detector is used as an advanced iterative MUD, the framework incorporates high-accuracy MI prediction based on VSS, utilizing VDB and ANN search, thereby reflecting iterative detection gains in MCS selection. The key advantage of the proposed framework is its applicability to any MUD scheme whose decoder input cannot be analytically derived. Computer simulation results verify the effectiveness of the proposed method from both system and user throughput perspectives in a setup compliant with the 5G NR standard. The results demonstrate that the proposed MCS selection framework can effectively translate the performance gains of advanced iterative detectors into tangible system-level improvements and that it can significantly enhance reliability and spectral efficiency.

## REFERENCES

- [1] H. Tataria, M. Shafi, A. F. Molisch, M. Dohler, H. Sjöland, and F. Tufvesson, "6G wireless systems: Vision, requirements, challenges, insights, and opportunities," *Proc. IEEE*, vol. 109, no. 7, pp. 1166–1199, 2021.
- [2] W. Jiang, B. Han, M. A. Habibi, and H. D. Schotten, "The road towards 6G: A comprehensive survey," *IEEE Open J. Commun. Soc.*, vol. 2, pp. 334–366, 2021.
- [3] W. Chen, X. Lin, J. Lee, A. Toskala, S. Sun, C. F. Chiasserini, and L. Liu, "5G-advanced toward 6G: Past, present, and future," *IEEE J. Sel. Areas Commun.*, vol. 41, no. 6, pp. 1592–1619, 2023.
- [4] A. Hussein, P. Mitran, and C. Rosenberg, "Operating multi-user massive MIMO networks: Trade-off between performance and runtime," *IEEE Trans. Netw. Service Manag.*, vol. 21, no. 2, pp. 2170–2186, 2024.
- [5] K. Ito, T. Takahashi, K. Ishibashi, K. Igarashi, and S. Ibi, "Joint channel, CFO, and data estimation via Bayesian inference for multi-user MIMO-OFDM systems," *IEEE Trans. Wireless Commun.*, vol. 24, no. 3, pp. 1898–1915, 2025.
- [6] K. Ito, T. Takahashi, K. Ishibashi, S. Ibi, and H. Ochiai, "Cross-domain joint channel and data estimation for mmwave MIMO-OFDM systems with low-resolution ADCs," *IEEE J. Sel. Top. Signal Process.*, vol. 19, no. 6, pp. 1009–1025, 2025.
- [7] A. Chockalingam and B. S. Rajan, *Large MIMO Systems*. Cambridge University Press, 2014.
- [8] S. Yang and L. Hanzo, "Fifty years of MIMO detection: The road to large-scale MIMOs," *IEEE Commun. Surveys Tuts.*, vol. 17, no. 4, pp. 1941–1988, 2015.
- [9] J. Céspedes, P. M. Olmos, M. Sánchez-Fernández, and F. Perez-Cruz, "Expectation propagation detection for high-order high-dimensional MIMO systems," *IEEE Trans. Commun.*, vol. 62, no. 8, pp. 2840–2849, Aug. 2014.
- [10] T. Takahashi, S. Ibi, and S. Sampei, "Design of adaptively scaled belief in multi-dimensional signal detection for higher-order modulation," *IEEE Trans. Commun.*, vol. 67, no. 3, pp. 1986–2001, Mar. 2019.

- [11] T. Furudoi, T. Takahashi, S. Ibi, and H. Ochiai, "Discrete-valued signal estimation via low-complexity message passing algorithm for highly correlated measurements," 2024. [Online]. Available: <https://arxiv.org/abs/2411.07558>
- [12] F. J. Martín-Vega, J. C. Ruiz-Sicilia, M. C. Aguayo, and G. Gómez, "Emerging tools for link adaptation on 5G NR and beyond: Challenges and opportunities," *IEEE Access*, vol. 9, pp. 126 976–126 987, 2021.
- [13] Q. An, M. Zafari, C. Dick, S. Segarra, A. Sabharwal, and R. Doost-Mohammady, "ML-based feedback-free adaptive MCS selection for massive multi-user MIMO," in *Proc. 57th Asilomar Conf. Signals Syst. Comput.*, 2023, pp. 157–161.
- [14] J. Shikida, N. Ishii, and Y. Kakura, "Performance analysis of low complexity multi-user MIMO scheduling schemes for massive MIMO system," in *Proc. 22nd Asia-Pacific Conf. Commun. (APCC)*, 2016, pp. 180–184.
- [15] T. Doi, J. Shikida, D. Shirase, K. Muraoka, N. Ishii, T. Takahashi, and S. Ibi, "Outer loop link adaptation based on user multiplexing for generalized approximate message passing in massive MIMO," in *Proc. IEEE Wireless Commun. Netw. Conf. (WCNC)*, 2024, pp. 1–6.
- [16] K. P. Srinath and J. Hoydis, "Bit-metric decoding rate in multi-user MIMO systems: Theory," *IEEE Trans. Wireless Commun.*, vol. 22, no. 11, pp. 7961–7974, 2023.
- [17] A. M. Cipriano, R. Visoz, and T. Salzer, "Calibration issues of PHY layer abstractions for wireless broadband systems," in *Proc. IEEE Veh. Technol. Conf. (VTC Fall)*, 2008, pp. 1–5.
- [18] J. Francis and N. B. Mehta, "EESM-based link adaptation in point-to-point and multi-cell OFDM systems: Modeling and analysis," *IEEE Trans. Wireless Commun.*, vol. 13, no. 1, pp. 407–417, 2014.
- [19] IEEE, "IEEE standard for information technology—telecommunications and information exchange between systems local and metropolitan area networks—specific requirements - part 11: Wireless LAN medium access control (MAC) and physical layer (PHY) specifications," *IEEE Std 802.11-2016 (Revision of IEEE Std 802.11-2012)*, pp. 1–3534, 2016.
- [20] 3GPP, "LTE; evolved universal terrestrial radio access (E-UTRA); multiplexing and channel coding," 3GPP, TS 38.212, 2022, v17.1.0.
- [21] —, "5G; NR; multiplexing and channel coding," 3GPP, TS 38.212, 2024, v18.4.0.
- [22] K. K. Sayana, J. Zhuang, and K. A. Stewart, "Link performance abstraction based on mean mutual information per bit (MMIB) of the LLR channel," in *IEEE Standard 802.16 Broadband Wireless Access Working Group.*, 2007.
- [23] T. L. Jensen, S. Kant, J. Wehinger, and B. H. Fleury, "Fast link adaptation for MIMO OFDM," *IEEE Trans. Veh. Technol.*, vol. 59, no. 8, pp. 3766–3778, 2010.
- [24] X. Hu and X. Dai, "PER prediction in MIMO-OFDM systems with approximate demodulation: A GMI-based method," *IEEE Trans. Veh. Technol.*, vol. 72, no. 9, pp. 11 548–11 557, 2023.
- [25] T. P. Minka, "Expectation propagation for approximate Bayesian inference," *Computing Research Repository (CoRR)*, vol. abs/1301.2294, 2013. [Online]. Available: <http://arxiv.org/abs/1301.2294>
- [26] S. Rangan, P. Schniter, and A. K. Fletcher, "Vector approximate message passing," *IEEE Trans. Inf. Theory*, vol. 65, no. 10, pp. 6664–6684, 2019.
- [27] K. Takeuchi, "Rigorous dynamics of expectation-propagation-based signal recovery from unitarily invariant measurements," *IEEE Trans. Inf. Theory*, vol. 66, no. 1, pp. 368–386, 2020.
- [28] F. Kobayashi, T. Takahashi, S. Ibi, H. Ochiai, K. Muraoka, T. Doi, and N. Ishii, "Vector similarity search-based MCS selection for iterative signal detection in massive multi-user MIMO-OFDM systems," in *Proc. IEEE Wireless Commun. Netw. Conf. (WCNC)*, 2025, pp. 1–6.
- [29] H. Wang, A. Kosasih, C.-K. Wen, S. Jin, and W. Hardjawana, "Expectation propagation detector for extra-large scale massive MIMO," *IEEE Trans. Wireless Commun.*, vol. 19, no. 3, pp. 2036–2051, 2020.
- [30] R. Tamaki, K. Ito, T. Takahashi, S. Ibi, and S. Sampei, "Suppression of self-noise feedback in GAMP for highly correlated large MIMO detection," in *Proc. IEEE Int. Conf. Commun. (ICC)*, 2022, pp. 1300–1305.
- [31] T. Takahashi, A. Tölli, S. Ibi, and S. Sampei, "Low-complexity large MIMO detection via layered belief propagation in beam domain," *IEEE Trans. Wireless Commun.*, vol. 21, no. 1, pp. 234–249, 2022.
- [32] Y. Cao, H. Qi, W. Zhou, J. Kato, K. Li, X. Liu, and J. Gui, "Binary hashing for approximate nearest neighbor search on big data: A survey," *IEEE Access*, vol. 6, pp. 2039–2054, 2018.
- [33] J. Johnson, M. Douze, and H. Jégou, "Billion-scale similarity search with GPUs," *IEEE Trans. Big Data*, vol. 7, no. 3, pp. 535–547, 2019.
- [34] J. J. Pan, J. Wang, and G. Li, "Survey of vector database management systems," *Vldb J.*, vol. 33, no. 5, pp. 1591–1615, 2024.
- [35] M. Douze, A. Guzhva, C. Deng, J. Johnson, G. Szilvasy, P.-E. Mazaré, M. Lomeli, L. Hosseini, and H. Jégou, "The Faiss library," *IEEE Trans. Big Data*, pp. 1–17, 2025.
- [36] W. Jianguo *et al.*, "Milvus: A purpose-built vector data management system," in *Proc. Int. Conf. Manage. Data*, 2021, pp. 2614–2627.
- [37] W. Zhao, S. Tan, and P. Li, "Song: Approximate nearest neighbor search on gpu," in *Proc. IEEE 36th Int. Conf. Data Eng. (ICDE)*, 2020, pp. 1033–1044.
- [38] Z. Yang, A. Nakai-Kasai, and T. Wadayama, "Approximate nearest search with vector databases for power allocation in interference channels," in *Proc. 46th SITA*, 2023, pp. 238–243.
- [39] L. Wei, T. Wadayama, and K. Hayashi, "Vector similarity search based offline learning for deep-unfolded MIMO signal detector," in *Proc. IEEE Int. Conf. Mach. Learn. Commun. Netw. (ICMLCN)*, 2024, pp. 7–12.
- [40] S. ten Brink, "Convergence behavior of iteratively decoded parallel concatenated codes," *IEEE Trans. Commun.*, vol. 49, no. 10, pp. 1727–1737, 2001.
- [41] J. Hagenauer, "The EXIT chart - Introduction to extrinsic information transfer in iterative processing," in *Proc. 12th European Signal Process. Conf.*, 2004, pp. 1541–1548.
- [42] R. Bruno, A. Masaracchia, and A. Passarella, "Robust adaptive modulation and coding (AMC) selection in lte systems using reinforcement learning," in *Proc. IEEE Veh. Technol. Conf. (VTC Fall)*, 2014, pp. 1–6.
- [43] M. P. Mota, D. C. Araujo, F. H. Costa Neto, A. L. F. de Almeida, and F. R. Cavalcanti, "Adaptive modulation and coding based on reinforcement learning for 5G networks," in *Proc. IEEE Global Commun. Conf. (GLOBECOM) WS*, 2019, pp. 1–6.
- [44] N. C. Luong, D. T. Hoang, S. Gong, D. Niyato, P. Wang, Y.-C. Liang, and D. I. Kim, "Applications of deep reinforcement learning in communications and networking: A survey," *IEEE Commun. Surveys Tuts.*, vol. 21, no. 4, pp. 3133–3174, 2019.
- [45] L. Zhang, J. Tan, Y.-C. Liang, G. Feng, and D. Niyato, "Deep reinforcement learning-based modulation and coding scheme selection in cognitive heterogeneous networks," *IEEE Trans. Wireless Commun.*, vol. 18, no. 6, pp. 3281–3294, 2019.
- [46] X. Ye, Y. Yu, and L. Fu, "Deep reinforcement learning based link adaptation technique for LTE/NR systems," *IEEE Trans. Veh. Technol.*, vol. 72, no. 6, pp. 7364–7379, 2023.
- [47] Y. Liao, Z. Yang, Z. Yin, and X. Shen, "DQN-based adaptive MCS and SDM for 5G massive MIMO-OFDM downlink," *IEEE Commun. Lett.*, vol. 27, no. 1, pp. 185–189, 2023.
- [48] 3GPP, "5G; NR; physical channels and modulation," 3GPP, TS 38.211, 2024, v18.4.0.
- [49] F. Kobayashi, T. Takahashi, S. Ibi, and H. Ochiai, "EXIT chart analysis of expectation propagation-based iterative detection and decoding," *IEEE Open J. Commun. Soc.*, vol. 6, pp. 5249–5268, 2025.
- [50] S. Ibi, T. Matsumoto, R. Thomä, S. Sampei, and N. Morinaga, "EXIT chart-aided adaptive coding for multilevel BICM with turbo equalization in frequency-selective MIMO channels," *IEEE Trans. Veh. Technol.*, vol. 56, no. 6, pp. 3757–3769, Nov. 2007.
- [51] A. Paulraj, R. Nabar, and D. Gore, *Introduction to Space-Time Wireless Communications*, 1st ed. USA: Cambridge University Press, 2008.
- [52] A. Ashikhmin, G. Kramer, and S. ten Brink, "Extrinsic information transfer functions: model and erasure channel properties," *IEEE Trans. Inf. Theory*, vol. 50, no. 11, pp. 2657–2673, 2004.
- [53] E. Sharon, A. Ashikhmin, and S. Litsyn, "Analysis of low-density parity-check codes based on EXIT functions," *IEEE Trans. Commun.*, vol. 54, no. 8, pp. 1407–1414, 2006.
- [54] 3GPP, "5G; study on channel model for frequencies from 0.5 to 100 GHz," 3GPP, TR 38.901, 2024, v18.0.0.
- [55] —, "5G; NR; physical layer procedures for data," 3GPP, TS 38.214, 2024, v18.4.0.
- [56] J. Sivic and A. Zisserman, "Video Google: a text retrieval approach to object matching in videos," in *Proc. IEEE Int. Conf. Comput. Vis.*, 2003, pp. 1470–1477 vol.2.
- [57] H. Jégou, M. Douze, and C. Schmid, "Product quantization for nearest neighbor search," *IEEE Trans. Pattern Anal. Mach. Intell.*, vol. 33, no. 1, pp. 117–128, 2011.
- [58] A. Durán, M. Toril, F. Ruiz, and A. Mendo, "Self-optimization algorithm for outer loop link adaptation in LTE," *IEEE Commun. Lett.*, vol. 19, no. 11, pp. 2005–2008, 2015.
- [59] E. Peralta, G. Pocovi, L. Kuru, K. Jayasinghe, and M. Valkama, "Outer loop link adaptation enhancements for ultra reliable low latency communications in 5G," in *Proc. IEEE 95th Veh. Technol. Conf. (VTC Spring)*, 2022, pp. 1–7.
- [60] M. Liu, J. Chen, G. Wu, L. Ji, and H. Wang, "Soft-ACK based outer loop link adaptation for latency-constrained 5G video conferencing," in *Proc. IEEE Global Commun. Conf. (GLOBECOM)*, 2023, pp. 388–393.
- [61] K. Hashimoto, F. Kobayashi, T. Takahashi, S. Ibi, K. Muraoka, T. Doi, and H. Ochiai, "Low-complexity MCS selection via vector similarity search for multi-user MIMO systems," in *Proc. IEEE Global Commun. Conf. (GLOBECOM) WS*, 2025, pp. 1–6.